

# Atmospheric and adaptive optics

**Paul Hickson**

Received: 17 June 2014 / Published online: 1 November 2014  
© Springer-Verlag Berlin Heidelberg 2014

**Abstract** Atmospheric optics is the study of optical effects induced by the atmosphere on light propagating from distant sources. Of particular concern to astronomers is atmospheric turbulence, which limits the performance of ground-based telescopes. The past two decades have seen remarkable growth in the capabilities and performance of adaptive optics (AO) systems. These opto-mechanical systems actively compensate for the blurring effect of the Earth's turbulent atmosphere. By sensing, and correcting, wavefront distortion introduced by atmospheric index-of-refraction variations, AO systems can produce images with resolution approaching the diffraction limit of the telescope at near-infrared wavelengths. This review highlights the physical processes and fundamental relations of atmospheric optics that are most relevant to astronomy, and discusses the techniques used to characterize atmospheric turbulence. The fundamentals of AO are then introduced and the many types of advanced AO systems that have been developed are described. The principles of each are outlined, and the performance and limitations are examined. Aspects of photometric and astrometric measurements of AO-corrected images are considered. The paper concludes with a discussion of some of the challenges related to current and future AO systems, particularly those that will equip the next generation of large, ground-based optical and infrared telescopes.

**Keywords** Atmospheric effects · Instrumentation: adaptive optics · Instrumentation: high angular resolution · Site testing · Techniques: high angular resolution

---

P. Hickson (✉)

Department of Physics and Astronomy, The University of British Columbia, 6224 Agricultural Road, Vancouver, BC V6T 1Z1, Canada  
e-mail: hickson@physics.ubc.ca

## 1 Introduction

For three centuries, astronomical observations using ground-based optical telescopes have been limited by atmospheric “seeing”, a term used by astronomers to describe the image blurring caused by the atmosphere. Seeing results from the imperfect focussing of wavefronts distorted by phase fluctuations that occur as the light propagates through regions of differing index of refraction in a turbulent atmosphere. At good astronomical sites, seeing limits the resolution of ground-based telescopes to about 1 arcsec at optical wavelengths, regardless of telescope diameter.

[Babcock \(1953\)](#) was the first to suggest that atmospheric phase fluctuations could in principle be compensated by sensing the wavefront phase using light from a reference star, and then correcting the phase fluctuations by means of a deformable mirror. However, it was not until the 1980’s that technical progress made this idea of “adaptive optics” (AO) feasible. More detail on the historical context can be found in [Roddier \(1999\)](#) and [Duffner \(2009\)](#). Today, AO is an essential technology employed by major observatories worldwide. Many types of AO systems have been developed, each addressing a different range of science programs and telescope configurations. As a result, ground-based telescopes can now achieve a resolution comparable to, and sometimes exceeding, that of space telescopes ([Fig. 1](#)).

The theoretical basis of AO has also undergone rapid development, beginning with the seminal work of [Tatarskii \(1961\)](#) on the propagation of light through a turbulent medium. A comprehensive review of the effects of atmospheric optics in an astronomical context can be found in [Roddier \(1981\)](#), and a useful compilation of recent articles is given by [Businger and Cherubini \(2011\)](#). An early review of AO was given by [Beckers \(1993a\)](#). Introductory books on adaptive optics include [Hardy \(1998\)](#) and [Tyson \(2000\)](#). Advanced texts include [Lukin \(1996\)](#), [Roggeman and Welsh \(1996\)](#), [Kibble-](#)

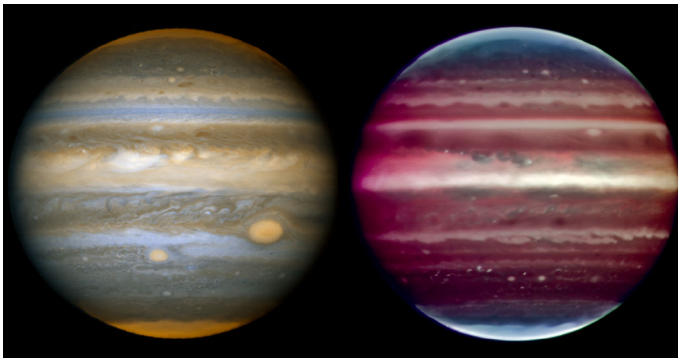


**Fig. 1** Visible-light image of Jupiter (*left*), taken by the Hubble Space Telescope (HST) is compared with an infrared image (*right*), obtained with the MAD multi-conjugate adaptive optics system on ESO’s Very Large Telescope. The AO-corrected ground-based image, which is a composite of exposures taken on 17 August 2008 at 2, 2.14 and 2.16  $\mu\text{m}$  wavelengths, has a spatial resolution of 90 milli-arcsec, comparable to that of the HST image. The HST image was taken on 16 April 2006 and is a composite of exposures taken at 0.502 and 0.892  $\mu\text{m}$  wavelengths. [NASA, ESA, I. de Pater and M. Wong (University of California, Berkeley); ESO/F. Marchis, M. Wong, E. Marchetti, P. Amico, S. Tordo]

white and Wild (2006), Sasiela (2007) and Tyson (2011). Sasiela (2007) provides a comprehensive development of adaptive optics theory. Convenient summaries of the relevant equations for atmospheric propagation and AO are given by Andrews (2004) and Tyson and Frazier (2004) respectively. Andrews and Phillips (2005) provides a detailed review of the physics of propagation in turbulence. Comprehensive introductions to the concepts of optical coherence and statistics can be found in Goodman (1985) and Mandel and Wolf (1995). An excellent recent review of adaptive optics from an astrophysical perspective is given by Davies and Kasper (2012). Recent developments in the field are highlighted in the biennial conferences “Adaptive optics for Extremely Large Telescopes” (Clénet et al. 2010; Véran et al. 2012; Esposito and Fini 2013).

## 2 Theoretical background

Atmospheric turbulence is generated by mechanical processes and thermal instability. Wind flowing over topographic features creates downwind turbulence that can persist for many kilometers. On a smaller scale, obstructions, trees, and man-made structures create local mechanical turbulence. Daytime heating produces thermal instability that leads to convective turbulence in the lower atmosphere. Wind shear associated with airflow aloft, such as jet streams, results in high-altitude turbulence. In each case, turbulent flow mixes air of different temperatures. The index of refraction  $N$  of air is a function primarily of density  $\rho$ , which is related to temperature  $T$  and pressure  $P$  by the ideal gas law,  $P \propto \rho T$ . Thus  $\delta \ln(N - 1) = \delta \ln(P) - \delta \ln(T)$ . Pressure fluctuations are negligible for velocities that are much lower than the sound speed, so temperature fluctuations are the dominant factor. It follows that  $\delta N \simeq -(N - 1)\delta T/T$ . In the lower atmosphere,  $N - 1 \simeq 3 \times 10^{-4}$  and local root-mean-square (RMS) air temperature fluctuations on the scale of a metre are typically on the order of 0.1 C. Thus, RMS index of refraction variations on this scale are at a level of about  $10^{-7}$ .

The cumulative effect of such fluctuations on propagating light is substantial. As turbulent air is carried across the light propagation path by the prevailing wind, fluctuations develop in both the phase and amplitude of light reaching the telescope, which give rise to the phenomena of seeing and scintillation, respectively.

### 2.1 The turbulence spectrum

Our understanding of turbulence stems from the concept of a turbulent cascade, first described by Richardson (1922). Richardson’s key insight was that the movement of air produces large eddies, which in turn produce smaller eddies, transporting energy from larger to smaller scales. Energy is injected at an outer scale, comparable to the thickness of the turbulent layer, and is dissipated at an inner scale by viscous forces. At typical astronomical sites, the outer scale is on the order of a few metres and the inner scale is a few millimetres. In the “inertial range” between these two scales, the turbulent flow is largely isotropic and self-similar. This was quantified by Kolmogorov (1941) and Obukhov (1941a), who reasoned that the statistical properties of the flow can depend only on the length scale  $r$  and the rate of energy dissipation per unit mass  $\varepsilon$ .

At any point, fixed in space, the mean value of the velocity fluctuation is zero, but the mean square difference in velocity between two points increases with their separation. This quantity,  $\mathcal{D}_v(\mathbf{r}) = \langle [v(\mathbf{x}) - v(\mathbf{x} + \mathbf{r})]^2 \rangle$ , is called the velocity structure function. Here, the brackets denote an ensemble average. The only combination of  $\varepsilon$  and  $r$  having dimensions of velocity is  $(\varepsilon r)^{1/3}$ , so the structure function must be proportional to  $r^{2/3}$  and, for isotropic turbulence, independent of the direction of  $\mathbf{r}$ .

Obukhov (1941b) and Yaglom (1941) showed that physical properties carried passively by the flow, such as temperature, must satisfy the same scaling relation. Therefore, the structure function of index-of-refraction fluctuations  $n = N - 1$  also obeys the Kolmogorov–Obukhov scaling law

$$\mathcal{D}_n(r) = C_n^2 r^{2/3}. \quad (1)$$

The proportionality constant  $C_n^2$ , is called the index of refraction structure constant. It characterizes the strength of the turbulence and is a key parameter determining seeing, and the performance of AO systems.

It is often convenient to work in the spectral domain, in which fluctuations are characterized by spatial scale, or its reciprocal, the wave number or spatial frequency  $\kappa$ . For isotropic turbulence, the structure function is related to the power spectral density (PSD) of index of refraction fluctuations,  $\Phi_n(\kappa)$ , by

$$\mathcal{D}_n(r) = 8\pi \int \Phi_n(\kappa) \left[ 1 - \frac{\sin(\kappa r)}{(\kappa r)} \right] \kappa^2 d\kappa, \quad (2)$$

where  $\kappa$  is the modulus of the three-dimensional spatial frequency vector  $\boldsymbol{\kappa}$ .

The PSD that gives the structure function of Eq. (1) is

$$\Phi_n(\kappa) = 0.0330 C_n^2 \kappa^{-11/3}, \quad (3)$$

The numerical constant is more precisely  $\Gamma(8/3) \sin(\pi/3)/(4\pi^2)$  (Roddiier 1981). This is the Kolmogorov spectrum.

An important generalization that includes a cutoff at an outer scale  $L_0$  is the von Karman spectrum

$$\Phi_n(\kappa) = 0.0330 C_n^2 (\kappa^2 + \kappa_0^2)^{-11/6}, \quad (4)$$

where  $\kappa_0 = 2\pi/L_0$ .

## 2.2 Optical propagation through a turbulent atmosphere

In order to better understand seeing and AO, it will be helpful to first review the physics of light passing through a turbulent atmosphere. An exact theory of propagation of electromagnetic waves in a turbulent medium remains an unsolved problem. However, approximate solutions have been found that are valid for most situations encountered with AO on large telescopes. In this section we outline one theoretical approach, and the principal results.

Atmospheric turbulence has no direct effect on the polarization of light, so it is sufficient to consider only the amplitude of the electric vector  $E$ , which satisfies the scalar wave equation

$$\left( \nabla^2 - \frac{N^2}{c^2} \frac{\partial^2}{\partial t^2} \right) E(\mathbf{r}, t) = 0, \quad (5)$$

the substitution  $E(\mathbf{r}, t) = \Psi(\mathbf{r}) \exp[i(\mathbf{k} \cdot \mathbf{r} - \omega t)]$  results in

$$\left\{ \nabla^2 + 2i\mathbf{k} \cdot \nabla + k^2[N(\mathbf{r})^2 - 1] \right\} \Psi(\mathbf{r}) = 0, \quad (6)$$

where the wave vector  $\mathbf{k}$  points in the direction of propagation and has amplitude  $k = 2\pi/\lambda = \omega/c$ .  $\Psi$  is the complex amplitude of the electromagnetic field.

Now redefine  $\mathbf{r}$  to be a two-dimensional vector transverse to the direction of propagation  $z$ , and  $\boldsymbol{\kappa}$  as the corresponding two-dimensional spatial frequency vector. The Laplacian operator can be separated into transverse  $\nabla_r^2$  and longitudinal components, giving

$$\left[ \nabla_r^2 + \frac{\partial^2}{\partial z^2} + 2ik \frac{\partial}{\partial z} + k^2(N^2 - 1) \right] \Psi(\mathbf{r}, z) = 0. \quad (7)$$

The amplitude  $\Psi(\mathbf{r}, z)$  changes very little while propagating a distance  $\lambda$ , so the second term in this equation is much smaller than the third and can generally be neglected. This is the paraxial, or Fresnel, approximation. Also, since  $n = N - 1 \ll 1$ ,  $N^2 - 1 \simeq 2n$ . This gives the “paraxial” wave equation

$$\left[ 2ik \frac{\partial}{\partial z} + \nabla_r^2 + 2k^2 n(\mathbf{r}) \right] \Psi(\mathbf{r}, z) = 0. \quad (8)$$

To solve this equation one needs complete knowledge of the index of refraction throughout the volume. However, in many cases we are interested only in statistical properties of the radiation field at the position of the observer or telescope. These can be related to the statistics of the index-of-refraction fluctuations, namely, the turbulence strength and spectrum.

The simplest statistic is the first-order coherence function  $\Gamma_1$ . This is defined as the mean value of the field  $\Psi$ , and can be determined exactly from Eq. (8). If  $\Psi_0$  is the field at the top of the atmosphere, the mean field after propagation to the telescope (located at  $z = 0$ ), is given by

$$\Gamma_1 \equiv \langle \Psi \rangle = \Psi_0 \exp \left[ -2\pi^2 k^2 \int_0^\infty dz \int_0^\infty \Phi_n(\kappa, z) \kappa d\kappa \right]. \quad (9)$$

(Although the atmosphere has finite thickness, no error is introduced by allowing the integral over  $z$  to extend to infinity.) From Eq. (9) we see that as the wave propagates, the mean field decreases. This is a result of light being diffracted out of the beam by the refractive index inhomogeneities, which reduces the mean amplitude of the coherent

part of the radiation. The total energy is conserved, but the incoherent light is spread out over a larger angle.

It is useful to consider the effect on the amplitude and phase of the field separately. One introduces real variables  $\chi$  and  $\varphi$ , which correspond to log-amplitude and phase fluctuations respectively, according to the definition

$$\Psi(\mathbf{r}) = \Psi_0 \exp[\chi(\mathbf{r}) + i\varphi(\mathbf{r})]. \quad (10)$$

Initially, both  $\chi$  and  $\varphi$  are zero, but as the wave propagates through the atmosphere, fluctuations develop in both quantities. These are random variables in the sense that a different realization of the turbulence, having the same amplitude and spectrum, will result in different values of  $\chi$  and  $\varphi$ . At any location,  $\bar{\varphi} \equiv \langle \varphi \rangle$ , the mean value of the phase fluctuation  $\varphi$  averaged over many such realizations, will be zero. However, the mean value of  $\chi$  is not zero (Fried 1966). It follows from conservation of energy, the definition of irradiance, and Eq. (11) below, that  $\bar{\chi} = -\sigma_\chi^2$ , where  $\sigma_\chi^2$  is the variance of  $\chi$ .

Substituting Eq. (10) into Eq. (9) and using the relation

$$\langle \exp(x) \rangle = \exp \left[ \langle (x - \bar{x})^2 \rangle / 2 + \bar{x} \right], \quad (11)$$

valid for any Gaussian random variable  $x$ , we obtain an expression for the sum of the variances of the log-amplitude and phase fluctuations,

$$\sigma_\varphi^2 + \sigma_\chi^2 = 4\pi^2 k^2 \int_0^\infty dz \int_0^\infty \Phi_n(\kappa, z) \kappa d\kappa. \quad (12)$$

Further information can be found from the second-order coherence function, the mutual coherence  $\Gamma_2$ . This is defined to be the covariance between the values of the field measured at two positions  $\mathbf{r}_1$  and  $\mathbf{r}_2$  in the transverse plane. It also has an exact solution,

$$\begin{aligned} \Gamma_2(\mathbf{r}_1, \mathbf{r}_2) &\equiv \langle \Psi(\mathbf{r}_1) \Psi^*(\mathbf{r}_2) \rangle \\ &= I_0 \exp \left[ -4\pi^2 k^2 \int_0^\infty dz \int_0^\infty \Phi_n(\kappa, z) [1 - J_0(\kappa r)] \kappa d\kappa \right] \end{aligned} \quad (13)$$

where  $r = |\mathbf{r}_1 - \mathbf{r}_2|$ ,  $I_0 = |\Psi_0|^2$  and  $J_0$  is the Bessel function of the first kind.

Substituting from Eq. (10), as before, gives

$$\mathcal{D}_\chi(r) + \mathcal{D}_\varphi(r) = 8\pi^2 k^2 \int_0^\infty dz \int_0^\infty \Phi_n(\kappa, z) [1 - J_0(\kappa r)] \kappa d\kappa. \quad (14)$$

This result describes the spatial correlations of phase and log-amplitude fluctuations that develop as the wave propagates.

In order to separate these two types of fluctuations, we need the fourth-order coherence function

$$\begin{aligned}\Gamma_4(\mathbf{r}_1, \mathbf{r}_1, \mathbf{r}_2, \mathbf{r}_2) &\equiv \langle \Phi_n(\mathbf{r}_1) \Phi_n^*(\mathbf{r}_1) \Phi_n(\mathbf{r}_2) \Phi_n^*(\mathbf{r}_2) \rangle \\ &= \langle I(\mathbf{r}_1) I(\mathbf{r}_2) \rangle\end{aligned}\quad (15)$$

which describes the correlation of irradiance fluctuations (power per unit area)  $I \equiv \Psi \Psi^*$ . Analytic solutions have been found only in the limit of small fluctuations,  $\sigma_\chi^2 \lesssim 0.35$ . In this limit,

$$\begin{aligned}\langle I(\mathbf{r}_1) I(\mathbf{r}_2) \rangle &= I_0^2 \exp \left[ 16\pi^2 k^2 \int_0^\infty dz \int_0^\infty \kappa d\kappa \Phi_n(\kappa, z) J_0(\kappa r) \right. \\ &\quad \left. \times \sin^2(z\kappa^2/2k) \right].\end{aligned}\quad (16)$$

Substituting from Eq. (10) gives the covariance of  $\chi$ ,

$$\begin{aligned}\mathcal{C}_\chi(\mathbf{r}_1, \mathbf{r}_2) &\equiv \langle [\chi(\mathbf{r}_1) - \bar{\chi}] [\chi(\mathbf{r}_2) - \bar{\chi}] \rangle \\ &= 4\pi^2 k^2 \int_0^\infty dz \int_0^\infty \Phi(\kappa, z) \sin^2(z\kappa^2/2k) J_0(\kappa r) \kappa d\kappa,\end{aligned}\quad (17)$$

Since  $\mathcal{C}_\chi(0) = \sigma_\chi^2$ , Eqs. (17) and (12) give

$$\sigma_\chi^2 = 4\pi^2 k^2 \int_0^\infty dz \int_0^\infty \Phi(\kappa, z) \sin^2(z\kappa^2/2k) \kappa d\kappa, \quad (18)$$

$$\sigma_\varphi^2 = 4\pi^2 k^2 \int_0^\infty dz \int_0^\infty \Phi(\kappa, z) \cos^2(z\kappa^2/2k) \kappa d\kappa. \quad (19)$$

It follows from the definitions that the covariance and structure functions are related by

$$\mathcal{D}(\mathbf{r}_1, \mathbf{r}_2) = 2 [\mathcal{C}(0) - \mathcal{C}(\mathbf{r}_1, \mathbf{r}_2)]. \quad (20)$$

By combining Eqs. (14) and (17–20), one obtains the desired relations for the structure functions of log-amplitude and phase

$$\mathcal{D}_\chi(r) = 8\pi^2 k^2 \int_0^\infty dz \int_0^\infty \Phi(\kappa, z) [1 - J_0(\kappa r)] \sin^2(z\kappa^2/2k) \kappa d\kappa \quad (21)$$

$$\mathcal{D}_\varphi(r) = 8\pi^2 k^2 \int_0^\infty dz \int_0^\infty \Phi(\kappa, z) [1 - J_0(\kappa r)] \cos^2(z\kappa^2/2k) \kappa d\kappa \quad (22)$$

and, from Eqs. (19), (20) and (22), the phase covariance function

$$\mathcal{C}_\varphi(r) = 4\pi^2 k^2 \int_0^\infty dz \int_0^\infty \Phi(\kappa, z) \cos^2(z\kappa^2/2k) J_0(\kappa r) \kappa d\kappa. \quad (23)$$

Equations (21) and (22) show that intensity fluctuations increase with distance from the turbulence, while phase fluctuations are nearly independent of distance, provided that the spatial scale  $\kappa^{-1}$  is greater than the Fresnel length  $\sqrt{\lambda z}$ .

It is often sufficient to use the first-order approximation,  $\cos(z\kappa^2/2k) \simeq 1$  and  $\sin(z\kappa^2/2k) \simeq z\kappa^2/2k$ . This is called the near-field approximation. It is valid for most AO applications with large telescopes.

One generally assumes that the atmosphere is homogeneous in the horizontal plane, with variations occurring only with height  $h$ . One can then relate the range  $z$  to height from the zenith angle  $\zeta$  of the observation, since  $h = z \cos \zeta$ .

### 2.3 Seeing and scintillation

For the Kolmogorov turbulence spectrum of Eq. (3), Eq. (14) can be integrated to give

$$\mathcal{D}(r) \equiv \mathcal{D}_\varphi(r) + \mathcal{D}_\chi(r) = 6.884(r/r_0)^{5/3}. \quad (24)$$

The constant 6.884 is more accurately  $2[(24/5)\Gamma(6/5)]^{5/6}$ , and Fried's parameter  $r_0$  (Fried 1966) is defined by

$$r_0^{-5/3} = 0.423k^2 \int C_n^2(z) dz. \quad (25)$$

In practice, the log-amplitude structure function is usually much smaller than the phase structure function and can be neglected and Eq. (24) reduces to

$$\mathcal{D}_\varphi(r) \simeq 6.884(r/r_0)^{5/3}. \quad (26)$$

From this, we see that the Fried parameter is a characteristic transverse length scale at which the RMS phase difference, between two points on the wavefront, has reached 2.634 radians. Effectively, it is the scale over which phase fluctuations become decorrelated. This loss of coherence is the cause of astronomical seeing. It can be shown that, for telescopes having diameter  $D \gg r_0$ , the full-width at half-maximum intensity (FWHM) of a long-exposure image of a point source (the point-spread function or PSF) is

$$\epsilon \simeq 0.976\lambda/r_0. \quad (27)$$

We see from Eq. (25) that the Fried parameter is a function of wavelength,  $r_0 \propto \lambda^{6/5}$ , and thus  $\epsilon \propto \lambda^{-1/5}$ . Therefore, the seeing improves as wavelength increases. Also, we see that the Fried parameter is determined by the turbulence integral along the line of sight,

$$J = \int C_n^2(z) dz. \quad (28)$$



The distance to the turbulence has no consequence for seeing, but we shall see that it has an impact when considering AO performance over an extended field of view (FOV).

It follows from Eq. (21) that amplitude fluctuations increase with distance to the turbulence, on scales where diffraction is unimportant. These give rise to irradiance fluctuations that we observe as scintillation. Since irradiance  $I$  is the square of the amplitude,  $\delta \ln I = 2\delta\chi$ . Therefore the covariance of log irradiance fluctuations  $C_I$  is four times that of log amplitude fluctuations. Thus, from Eq. (17),

$$C_I(r) = 16\pi^2 k^2 \int dz \int \Phi_n(\kappa, z) \sin^2(z\kappa^2/2k) J_0(\kappa r) \kappa d\kappa. \quad (29)$$

For the von Karman spectrum (Eq. 4), this becomes

$$C_I(r) = \int C_n^2(z) K(r, z, \kappa_0) dz, \quad (30)$$

where

$$K(r, z, \kappa_0) = 0.8294k^2 \int (\kappa^2 + \kappa_0^2)^{-11/6} \sin^2(z\kappa^2/2k) J_0(\kappa r) \kappa d\kappa \quad (31)$$

represents the effect of a turbulent layer at range  $z$ .

The scintillation index is defined as the variance of  $\delta I/I$ . Setting  $r = 0$  in Eq. (29) gives

$$\sigma_I^2 = 16\pi^2 k^2 \int dz \int \Phi_n(\kappa, z) \sin^2(z\kappa^2/2k) \kappa d\kappa. \quad (32)$$

This equation breaks down if the fluctuations  $\delta I/I$  approach unity. Numerical analysis indicates that as the turbulence integral increases, the scintillation index reaches a peak and then drops, approaching a limiting value of 1. This limiting value corresponds to the case in which the positions of arriving photons are completely uncorrelated, whence  $\sigma_I^2 = 1$  follows directly from Gaussian statistics (Goodman 1985).

## 2.4 Zernike modes

It is useful to write the phase fluctuation in the telescope pupil as a superposition of orthogonal functions (modes). The Zernike functions, defined on the unit disk ( $r \leq 1$ ), are particularly convenient for circular pupils as the lowest orders match the classical Seidel aberrations of geometrical optics. One writes

$$\varphi(r, \phi) = \sum_{j=1}^{\infty} a_j Z_j(\rho, \phi) \quad (33)$$

where  $\rho = r/R$ ,  $R = D/2$  is the radius of the telescope aperture,  $a_j$  are coefficients, and  $Z_j(r, \phi)$  is the  $j$ -th Zernike function. Several different normalization and ordering conventions for Zernike functions are in use. We shall use that of Noll (1976), which is commonly used in the AO community.

The Zernike functions are orthogonal, satisfying

$$\int d^2\rho W(\rho) Z_j Z_k = \delta_{jk} \quad (34)$$

where the function  $W(\rho)$  is defined to equal  $1/\pi$  for  $\rho \leq 1$  and zero otherwise, and  $\delta_{jk}$  equals 1 if  $j = k$  and 0 otherwise. Using this property, we obtain the mode coefficients in terms of an integral over the wavefront phase,

$$a_j = \int d^2\rho \varphi(\rho, \phi) W(\rho) Z_j(\rho, \phi). \quad (35)$$

The first ten Zernike modes are shown in Table 1. The mean square wavefront phase error  $\langle \varphi^2 \rangle$ , averaged over the pupil, is given by the sum of the mean square values of the mode coefficients.

Noll (1976) has computed the variance of the coefficients  $a_j$  for a Kolmogorov turbulence spectrum. The variance of the first mode (piston) is infinite, but this mode corresponds to a constant phase (i.e. not a function of  $\mathbf{r}$ ), which has no effect on the image produced by the telescope. Removing this term results in a finite sum.

The residual phase variance, after removing the first  $k$  terms, is represented by

$$\langle \varphi^2 \rangle - \sum_{j=1}^k \langle |a_j|^2 \rangle = \Delta_k (D/r_0)^{5/3}, \quad (36)$$

where  $\Delta_k$  are constant coefficients whose values are listed in Table 1. From these we see that the (piston-removed) RMS phase error averaged over the pupil is 1.015 radians for a telescope having diameter  $r_0$  and is proportional to  $D^{5/6}$ . It can also be seen that 89 % of the total phase variance is contained in the wavefront tilt components alone.

The second and third Zernike modes correspond to wavefront tilt. Fluctuations in these modes create image motion in the telescope focal plane. The RMS angular displacement  $\sigma_\epsilon$  is related to RMS phase error  $\sigma_\varphi$  by

$$\sigma_\epsilon = \frac{\sigma_\varphi}{kD} \propto D^{-1/6}. \quad (37)$$

This shows that atmospheric image motion decreases as telescope aperture increases. A further reduction occurs if the telescope aperture becomes comparable to the outer scale of turbulence, as the variance then falls below the Kolmogorov result.

The Zernike functions can be written as a Fourier integral,

$$Z_j(\rho) W(\rho) = \frac{R^2}{4\pi^2} \int d^2\kappa G_j(\kappa R) \exp(-i\kappa \cdot \mathbf{r}) \quad (38)$$

**Table 1** The first ten Zernike modes

Mode	$n$	$m$	$G_k(\kappa R, \phi)$	Name	$\Delta_k$
$Z_1 = 1$	0	0	$2J_1(\kappa R)/\kappa R$	Piston	1.030
$Z_2 = 2\rho \cos \phi$	1	1	$4i \cos(\phi)J_2(\kappa R)/\kappa R$	Tilt	0.582
$Z_3 = 2\rho \sin \phi$	1	1	$4i \sin(\phi)J_2(\kappa R)/\kappa R$	Tilt	0.134
$Z_4 = \sqrt{3}(2\rho^2 - 1)$	2	0	$-2\sqrt{3}J_3(\kappa R)/\kappa R$	Focus	0.111
$Z_5 = \sqrt{6}\rho^2 \sin 2\phi$	2	2	$-2\sqrt{6} \sin(2\phi)J_3(\kappa R)/\kappa R$	Astigmatism	0.088
$Z_6 = \sqrt{6}\rho^2 \cos 2\phi$	2	2	$-2\sqrt{6} \cos(2\phi)J_3(\kappa R)/\kappa R$	Astigmatism	0.065
$Z_7 = \sqrt{8}(3\rho^3 - 2r) \sin \phi$	3	1	$-4\sqrt{2}i \sin(\phi)J_4(\kappa R)/\kappa R$	Coma	0.059
$Z_8 = \sqrt{8}(3\rho^3 - 2r) \cos \phi$	3	1	$-4\sqrt{2}i \cos(\phi)J_4(\kappa R)/\kappa R$	Coma	0.053
$Z_9 = \sqrt{8}\rho^3 \sin 3\phi$	3	3	$-4\sqrt{2}i \sin(3\phi)J_4(\kappa R)/\kappa R$	Trefoil	0.046
$Z_{10} = \sqrt{8}\rho^3 \cos 3\phi$	3	3	$-4\sqrt{2}i \cos(3\phi)J_4(\kappa R)/\kappa R$	Trefoil	0.040

$Z_k$  is the  $k$ th mode,  $n$  and  $m$  are the radial and azimuthal order numbers,  $G_k$  is the Fourier transform of the  $k$ th mode, and  $\Delta_k$  is the residual atmospheric phase variance coefficient, after removing the contributions from all modes up to and including  $k$  (Eq. 36)

where, following the convention of Sasiela (2007),

$$\begin{aligned} G_j(\kappa R) &= \int d^2\rho Z_j(\rho) W(\rho) \exp(i\kappa \cdot \mathbf{r}) \\ &= 2i^{2n-m} \sqrt{n+1} S_j(m, \phi) J_{n+1}(\kappa R)/\kappa R. \end{aligned} \quad (39)$$

Here  $S_j(m, \phi)$  equals  $\sqrt{2} \cos(m\phi)$  if  $j$  is even,  $\sqrt{2} \sin(m\phi)$  if  $j$  is odd, and 1 if  $m = 0$ . It is easily verified that

$$\sum_{j=1}^{\infty} |G_j(\kappa R)|^2 = 1. \quad (40)$$

The first ten transforms of the Zernike functions are listed in Table 1.

Many problems in AO can be cast in the form of an integral over spatial frequency of the product of the turbulence spectrum with “filter functions” that depend on the nature of the problem. As an example, consider two lines of sight through the atmosphere, to two stars having angular separation  $\alpha$ . The cross-covariance  $C_{jk}(\alpha)$  of the  $j$ -th Zernike coefficient for the wavefront phase from one star with the  $k$ -th coefficient for the wavefront from the second star can be written, using Eqs. (23), (35) and (38), as

$$\begin{aligned} C_{jk}(\alpha) &\equiv \langle a_j(0) a_k(\alpha) \rangle \\ &= 2\pi k^2 \int dz \int d^2\kappa \Phi(\kappa, z) G_j(\kappa R) G_k^*(\kappa R) \exp(iz\kappa \cdot \alpha) \\ &\quad \times \cos^2(\kappa^2 z/2k). \end{aligned} \quad (41)$$

A special case of this is the covariance of a single Zernike mode

$$\begin{aligned} C_{jj}(\alpha) &\equiv \langle a_j(0)a_k(\alpha) \rangle \\ &= 2\pi k^2 \int dz \int d^2\kappa \Phi(\kappa, z) |G_j(\kappa R)|^2 \cos(z\kappa \cdot \alpha) \cos^2(\kappa^2 z/2k). \end{aligned} \quad (42)$$

From Eqs. (20) and (42), the mean square phase difference, for Zernike mode  $j$ , between the two lines of sight is

$$\begin{aligned} D_{jj}(\alpha) &\equiv \langle [a_j(0) - a_j(\alpha)]^2 \rangle \\ &= 4\pi k^2 \int dz \int d^2\kappa \Phi(\kappa, z) |G_j(\kappa R)|^2 [1 - \cos(z\kappa \cdot \alpha)] \\ &\quad \times \cos^2(\kappa^2 z/2k). \end{aligned} \quad (43)$$

## 2.5 Coherence time and isoplanatic angle

The strength and distribution of atmospheric turbulence is of primary importance for AO. As we have seen, the integral of the turbulence profile gives Fried's parameter  $r_0$ , through Eq. (25). Two other important parameters used to characterize the atmosphere are the atmospheric coherence time (Roddier 1981),

$$\tau_0 = 0.314 \frac{r_0}{\bar{v}_{5/3}}, \quad (44)$$

and the isoplanatic angle,

$$\theta_0 = 0.314 \frac{r_0}{\bar{z}_{5/3}}, \quad (45)$$

where the bar and subscript denote a turbulence-weighted average,

$$\bar{x}_\mu \equiv \left[ \frac{1}{J} \int C_n^2(z) x^\mu dz \right]^{1/\mu}. \quad (46)$$

(The reason for the numerical coefficient will soon become clear.)

The factor that most affects the atmospheric coherence time is wind. To a good approximation, one can regard the turbulence in each layer of the atmosphere as fixed (on the short timescales relevant for AO), but moving through the telescope beam according to the wind at the corresponding altitude. This is the Taylor hypothesis (Taylor 1938), or the assumption of frozen flow, and is a good approximation in the troposphere on the relatively small horizontal scales sampled by telescope apertures. When the wind speed is high, turbulent eddies take less time to cross the telescope aperture, so the frequency of changes is high. Roughly, one would expect significant change in the time taken for the turbulence to move a distance  $r_0$ , so the frequency

**Table 2** Typical values of atmospheric coherence parameters

$\lambda$ ( $\mu\text{m}$ )	$r_0$ (m)	$\theta_0$ (arcsec)	$\tau_0$ (ms)
0.5	0.16	2.0	1.5
1.0	0.37	4.6	3.4
2.0	0.84	10.6	7.9

will be  $\sim v/r_0$ . Integrating over layers, and assuming a Kolmogorov spectrum, one obtains the Greenwood frequency ([Greenwood 1977](#))

$$f_G = 2.31\lambda^{-6/5} \left[ \sec \xi \int C_n^2(z) v^{5/3}(z) dz \right]^{3/5},$$

$$= 0.134/\tau_0. \quad (47)$$

Phase fluctuations resulting from propagation along two different lines of sight arriving at the observer at an angle  $\theta$ , become uncorrelated as  $\theta$  increases, an effect called angular anisoplanatism. The phase variance between the two lines of sight can be found from Eq. (43). The sum over all Zernike modes (including piston) gives the total phase variance. Making the near-field approximation, and using Eq. (40), we obtain

$$\begin{aligned} \sigma_\phi^2(\theta) &= 4\pi k^2 \int_0^\infty dz \int_0^\infty \kappa d\kappa \int_0^{2\pi} d\phi \Phi(\kappa, z) [1 - \cos(z\theta\kappa \cos \phi)] \\ &= 8\pi^2 k^2 \int_0^\infty dz \int_0^\infty \kappa d\kappa \Phi(\kappa, z) [1 - J_0(z\theta\kappa)]. \end{aligned} \quad (48)$$

For a Kolmogorov turbulence spectrum, this gives

$$\sigma_\phi^2(\theta) = (\theta/\theta_0)^{5/3}, \quad (49)$$

which shows that  $\theta_0$  is the angle for which the RMS phase difference is one radian.

Typical median values of  $r_0$ ,  $\tau_0$  and  $\theta_0$ , at the best astronomical sites, are listed in Table 2 ([Tokovinin et al. 2008](#); [Skidmore et al. 2009](#)).

### 3 Atmospheric measurements and models

A variety of instruments and techniques have been developed to measure seeing and turbulence profiles. Some of the more common techniques are discussed in the following sections.

#### 3.1 SCIDAR

Scintillation detection and ranging (SCIDAR, [Vernin and Roddier 1973](#)) is a powerful technique that uses light from a binary star to derive a profile of  $C_n^2$  as a function of

altitude. In a SCIDAR system, the light is focussed to form an image of the telescope pupil that is recorded by a high-speed electronic camera. Since the light from the two stars follows slightly different paths to the telescope, a single thin turbulent layer at range  $z$  will produce a double pattern of fluctuations separated in the pupil by the vector  $\boldsymbol{\rho} = z\boldsymbol{\alpha}$ , where  $\boldsymbol{\alpha}$  is the angular separation vector of the two stars. The two-dimensional autocovariance function of the pupil image will therefore have three peaks, corresponding to a shift of 0 and  $\pm z\boldsymbol{\alpha}$ .

For a continuous distribution of turbulence, the covariance of irradiance is given by the convolution of this pattern with the turbulence profile.

$$\mathcal{B}_{\mathcal{I}}(\mathbf{r}) = \frac{1}{(1+q)^2} \int dz C_n^2(z) [qK(\mathbf{r} + z\boldsymbol{\alpha}, z, \kappa_0) + qK(\mathbf{r} - z\boldsymbol{\alpha}, z, \kappa_0) + (1+q^2)K(\mathbf{r}, z, \kappa_0)]. \quad (50)$$

Here  $q$  is the flux ratio between the two stars. Since the functions  $K$  are known (Eq. 31), the turbulence profile,  $C_n^2(z)$ , can be estimated from the measured covariance by application of an inversion method such as maximum entropy or Markov-chain Monte Carlo techniques.

A limitation of conventional SCIDAR is that the irradiance fluctuations produced by a layer at range  $z$  are proportional to  $z^{5/6}$ , so turbulence near the telescope is difficult to detect. A variant, “Generalized SCIDAR”, overcomes this limitation by placing the imager at a position that is optically conjugate to a negative range (i.e. behind the telescope). This has the effect of increasing the distance between the turbulence and the imager plane, facilitating the sensing of low-altitude turbulence.

SCIDARs are capable of producing high-quality turbulence profiles for the entire troposphere. The vertical resolution is limited fundamentally by the intrinsic width of the covariance peak, which depends on the size of the telescope. Accordingly, telescopes having apertures of a metre or more are typically employed.

### 3.2 SLODAR

Slope Detection and Ranging (SLODAR: [Wilson 2002](#)) is similar to SCIDAR in that a double star is used to probe two lines of sight through the atmosphere. However in SLODAR, it is the local wavefront slope, rather than the intensity, that is measured in the pupil plane. The slope is measured separately for each star, from the positions of the centroids of the two star images in the subapertures of a Shack–Hartmann wavefront sensor (Sect. 4.2). For each subaperture, the cross-covariance of the wavefront slopes is computed and the average is compared with the prediction of Eq. (41), with  $R$  taken to be the radius of a subaperture, for an assumed turbulence spectrum and outer scale. For the wavefront tilt components there are three equations, for  $C_{11}$ ,  $C_{22}$  and  $C_{12}$ , from which one can obtain  $C_n^2(z)$  by inversion.

SLODAR provides a resolved turbulence profile in the lower atmosphere, to a range  $\sim D/\alpha$ , where  $\alpha$  is the double star separation and  $D$  is the telescope aperture diameter. The number of resolution elements in the profile is  $N - 1$ , where  $N$  is the number of subapertures across the pupil, in the direction of the binary star separation.

Refinements of the technique, to include effects of diffraction and improve resolution, are discussed by [Goodwin et al. \(2007\)](#).

### 3.3 MASS

The Multi-aperture Scintillation Sensor (MASS) is an instrument that provides a low-resolution turbulence profile for the upper part of the atmosphere, above 500 m ([Tokovinin 1988](#)). A single star is observed, and the scintillation is measured in the pupil plane of a small telescope. Because of diffraction, the intensity fluctuations produced by turbulence at high altitude spread spatially during propagation, according to Eq. (29). Thus, the covariance of the intensity field at ground level depends on the vertical distribution of turbulence. In the MASS instrument, photon counts are recorded in a series of concentric circular apertures. The covariance between the counts in these apertures can be predicted, for a given  $C_n^2$  profile, by convolving Eq. (29) with the spatial response functions of the apertures. Inversion then gives an estimate of turbulence integrals for, typically, six atmospheric layers ranging in altitude from 0.5 to 16 km ([Kornilov et al. 2003](#); [Tokovinin et al. 2003](#); [Tokovinin and Kornilov 2007](#)).

### 3.4 DIMM

The most commonly-used instrument for the measurement of seeing is the differential image motion monitor (DIMM). According to Eq. (37), the RMS angular displacement of a star image is proportional to the RMS phase error, which itself depends on  $r_0$ . However, other factors such as vibration, tracking errors and wind-shake all contribute to image motion. By measuring the differential motion of two images of the star, formed by two pupils separated by a distance  $d$ , these unwanted contributions can be rejected.

In the DIMM, a mask containing two circular apertures is placed in front of a small telescope. Each aperture produces an image of the star, and the two images are separated by means of an optical wedge inserted in one of the apertures. A series of short-exposure images are recorded by a CCD camera and the relative displacements of the centroids of two stellar images are measured. The phase variance of the differential wavefront tilt components for the two images is given by Eq. (43) with  $\alpha z$  replaced by  $\mathbf{d}$ ,

$$D_{jj}(\mathbf{d}) = 0.415k^2 J \int d^2\kappa (\kappa^2 + \kappa_0^2)^{-11/6} |G_j(R\kappa)|^2 [1 - \cos(\kappa \cdot \mathbf{d})]. \quad (51)$$

where  $j = 2, 3$ . The integral is readily computed for an assumed turbulence spectrum and aperture separation  $\mathbf{d}$ . Thus measurements of the tilt variance  $D_{22}$  and  $D_{33}$  in the directions parallel and perpendicular to  $\mathbf{d}$  give the turbulence integral  $J$ , through the entire atmosphere, which in turn gives the Fried parameter  $r_0$  via Eqs. (25) and (28).

DIMM measurements are insensitive to the outer scale, provided that  $d \ll L_0$ . However, they are affected by a number of intrinsic errors and biases ([Tokovinin 2002](#); [Kornilov et al. 2007](#)) and are sensitive to the turbulence spectral index, which may differ from the Kolmogorov value ([Berdja 2010](#)).

### 3.5 GSM

The Generalized Seeing Monitor (GSM: [Martin et al. 1994](#); [Ziad et al. 2000](#)) employs four telescopes of 10 cm aperture observing a single star. The tilt fluctuations of the wavefronts received by each telescope are recorded and the cross-covariances are computed for each baseline, as for the DIMM. The larger separations and the 6 independent baselines of the GSM, spanning several metres, allow it to measure, in addition to  $r_0$ , the outer scale  $L_0$ . Both GSM and DIMM can use stellar scintillation to estimate the isoplanatic angle  $\theta_0$ .

### 3.6 SHABAR

Scintillometers such as the “Shadow Band Array” (SHABAR) employ arrays of photodetectors that measure spatial correlations in scintillation of light from the Sun or Moon ([Beckers 1993b](#); [Hickson and Lanzetta 2004](#); [Tokovinin et al. 2010](#)). The irradiance received by each detector is recorded at high speed (typically  $\sim 1$  kHz). The variance, and the cross covariance between all pairs of detectors is computed and compared with Eq. (30), modified to include the effect of averaging by the finite angular size of the Sun or Moon,

$$K(r, z, \kappa_0) = 0.8294k^2 \int (\kappa^2 + \kappa_0^2)^{-11/6} \sin^2(\kappa^2 z / 2k) J_0(\kappa r) F(\kappa, z) \kappa d\kappa. \quad (52)$$

Here  $F(\kappa, z)$  is the squared modulus of the Fourier transform of the intensity-weighted beam cross section at range  $z$ . The  $C_n^2$  profile is obtained by inversion.

Lunar and solar SHABAR arrays are most sensitive to low-level turbulence, below about 1 km. At higher altitudes, the beam diameter for the sun or moon exceeds the outer scale and the scintillation signal is reduced. However, they are very effective at measuring surface-layer and dome turbulence and are relatively simple instruments that require little or no calibration. They were used extensively in the site test campaign for the Advanced Technology Solar Telescope ([Hill et al. 2006](#)), and have been employed for surface layer profiling and dome seeing measurements at several astronomical sites ([Lombardi et al. 2010](#); [Hickson et al. 2010](#)).

### 3.7 Atmospheric models

It is often useful to have an empirical model of atmospheric parameters relevant to AO. This includes typical profiles of  $C_n^2$  and also wind speed as a function of altitude for a given site. An early model for  $C_n^2$  is that of [Hufnagel and Stanley \(1964\)](#), which was based both on theoretical considerations and on measurements of the energy dissipation rate, and other mean atmospheric parameters, as a function of altitude. In this model,  $C_n^2$  follows an approximate power-law dependence from an altitude of 1 m to 40 km,

$$C_n^2 \simeq 8.2 \times 10^{-14} h^{-2/3}. \quad (53)$$



**Table 3** Atmospheric model coefficients

Model	$A \text{ (m}^{-2/3}\text{)}$	$B \text{ (m}^{-2/3}\text{)}$	$C \text{ (m}^{-2/3}\text{)}$	$h_0 \text{ (km)}$	$a_0 \text{ (km)}$
HVB 5/7	$1.7 \times 10^{-14}$	$2.7 \times 10^{-16}$	$3.59 \times 10^{-23}$	0.01	1.5
HVB-CP	$8.1 \times 10^{-15}$	$1.2 \times 10^{-14}$	$4.14 \times 10^{-23}$	0.03	0.5

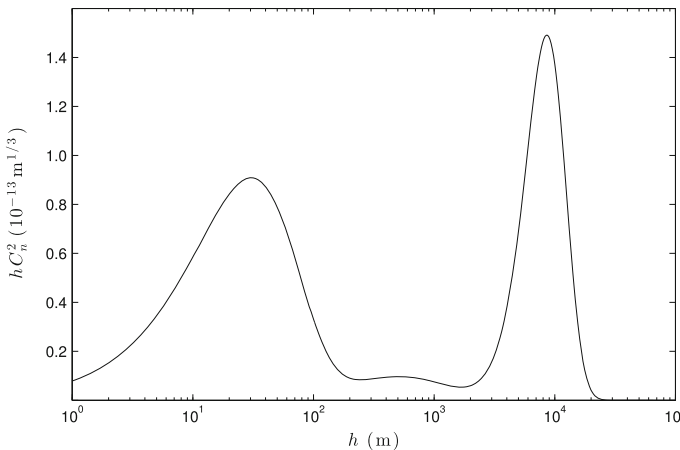


**Fig. 2** HVB atmospheric model, normalized using data from Cerro Pachón. The horizontal scale is height above the 2,722 m site. The vertical scale is chosen so that the area under the curve corresponds to the turbulence integral  $J$ , indicating the primary regions that contribute to the seeing. The low altitude peak corresponds to surface-layer turbulence in the lower  $\sim 100$  m and the  $\sim 10$  km peak corresponds to the high-altitude shear zone

A more general semi-empirical result that is widely used is the Hufnagel-Valley Boundary (HVB) model (Ulrich 1988), which has the form

$$C_n^2 \simeq A \exp(-h/h_0) + B \exp(-a/a_0) + C a^{10} \exp(-a) \quad (54)$$

where  $a$  is the altitude in km above mean sea level and  $h$  is the height in kilometers above the surface. Typical values for the coefficients  $A$ ,  $B$ ,  $C$ ,  $h_0$  and  $a_0$  are given in Table 3. The three terms correspond to a shallow “surface layer” contribution, a thicker “boundary layer” contribution, and a high-level shear-induced turbulent layer, respectively. Often, the first two terms are together referred to as the “ground layer” and the remaining higher-level turbulence is called the contribution of the “free atmosphere”.

In a study of turbulence profiles above Cerro Pachón (2,722 m altitude) Tokovinin and Travouillon (2006) employed a six-layer model for the free atmosphere and a double exponential for the ground layer. The median turbulence integrals for the free atmosphere and ground layer were found to be  $J_{FA} = 1.5 \times 10^{-13} \text{ m}^{1/3}$  and  $J_{GL} = 2.7 \times 10^{-13} \text{ m}^{1/3}$ . Thus, in median conditions the ground layer contributes 64 % of the total turbulence integral at this site. Coefficients of the HVB model that match the Cerro Pachón median ground-layer and free-atmosphere turbulence integral are given in Table 3 (denoted here by HVB-CP). This model is illustrated in Fig. 2.

These smooth models are an approximation to reality. Scidar measurements, and balloon-borne microthermal temperature soundings, show that the high-level turbulence is often confined to narrow atmospheric layers, and that the relative strength and altitude vary considerably. Nevertheless, smooth models are a useful tool in the prediction of telescope performance, with and without AO.

Recently, progress has been made towards predicting atmospheric turbulence from mesoscale atmospheric meteorological models (e.g. [Trinquet and Vernin 2006](#); [Hagelin et al. 2011](#)). With further development this may provide an effective tool for the planning of astronomical observations.

#### 4 Classical adaptive optics

In the simplest form of adaptive optics, light from a single reference star is used to sense the instantaneous atmospheric phase distortion. A deformable mirror (DM) is then adjusted to correct this phase distortion, converting the distorted wavefront into a nearly-plane wavefront. The correction is performed periodically, at a rate that is fast compared to the timescale of atmospheric phase variations. This sharpens the image of the reference star and also the images of objects that are close to it in the field of view. A system that uses a single DM is called a single-conjugate adaptive optics (SCAO) system.

Central to AO is the concept of subapertures. These are subdivisions of the pupil over which the wavefront phase error is averaged. They are required either by the discrete nature of the deformable mirror, which has a finite number of actuators, or by the need to average the signal from the reference star over a finite area in order to obtain sufficient signal-to-noise ratio.

One important measure of the performance of an AO system is the RMS wavefront phase error  $\sigma_\varphi$ , averaged over the telescope pupil. Since a constant phase has no effect on the image, and an overall wavefront tilt only displaces the image, not affecting the instantaneous image quality, the first three Zernike modes (piston and tilt) are generally not included in  $\sigma_\varphi$ . (It is nevertheless necessary to actively compensate the wavefront tilt modes in order to stabilize the image for any exposures that are longer than a few milliseconds.) Often,  $\sigma_\varphi$  is expressed in terms of the equivalent optical path length  $\sigma_l = \sigma_\varphi/k$ , with units of nm. Because the path-length error induced by the atmosphere does not depend strongly on wavelength over the bands used for AO,  $\sigma_l$  is nearly independent of wavelength.

A related and widely used measure of the quality of the AO image is the Strehl ratio  $S$ . This is defined as the ratio of the central intensity of the point spread function (PSF) to that of a perfect diffraction-limited PSF. For well-corrected images, the Maréchal approximation ([Maréchal 1947](#)) can be used to relate the Strehl ratio to the RMS phase error,

$$S \simeq \exp(-\sigma_\varphi^2) \quad (55)$$

Current AO systems can achieve Strehl ratios of  $\sim 50\%$  or greater under typical atmospheric conditions.

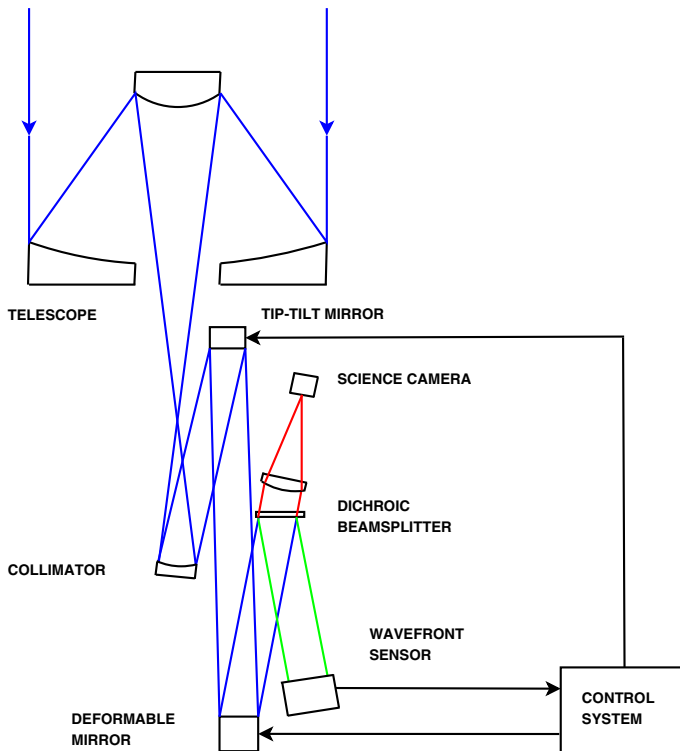


**Fig. 3** Schematic diagram of a single-conjugate AO system. Light from the reference star is shown in *green* and from the science target in *red*. *Blue lines* indicate the combination of the two

#### 4.1 AO system components and layout

In a SCAO system, a collimator, located after the telescope focus, forms an image of the telescope entrance pupil (Fig. 3). A DM is placed at this location, and the light reflected from this mirror is re-imaged onto the “science” detector. A portion of the reflected light is extracted by a beamsplitter and directed to a wavefront sensor. The wavefront sensor produces a signal that encodes the departure of the wavefront from a reference plane wave. This signal is processed by a control system, which then adjusts the surface figure of the DM in order to reduce the wavefront error. It is important to note that this is a closed-loop feedback system, in which the quality of the correction is monitored by the wavefront sensor and continuously refined by the control system. We shall see in Sect. 5 that some wide-field AO systems employ open-loop architectures, in which the required DM shape is predicted, but not monitored by sensing the corrected wavefront.

A separate tip-tilt mirror is normally employed to reduce the stroke (displacement) that the deformable mirror must provide. This mirror pivots on two orthogonal axes and is usually piezoelectrically controlled.

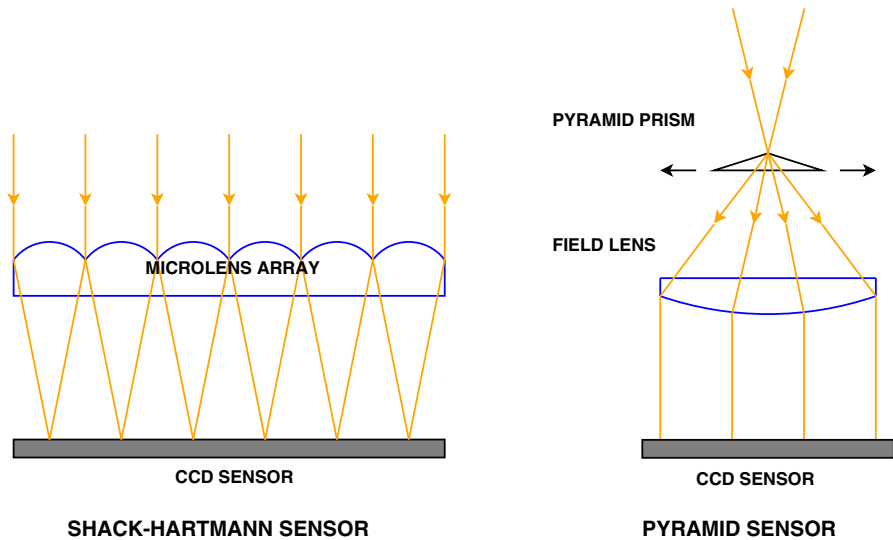


**Fig. 4** Schematic of Shack–Hartmann and pyramid wavefront sensors

## 4.2 Wavefront sensing techniques

Arguably, the most common wavefront sensor (WFS) in use is the Shack–Hartmann sensor. This sensor employs a rectangular array of small lenses (a “lenslet array”), placed in the plane of the pupil image (Fig. 4). These lenslets define the subapertures of the system. Each produces an image of the reference star. The position of the centroid of the image is determined by the local slope of the wavefront, averaged over the subaperture,  $\mathbf{x} = f\nabla\varphi/k$ , where  $f$  is the focal length of the lenslet and  $\mathbf{x}$  is the displacement of the image centroid from the nominal (no phase error) position. By integrating the measured gradients, the phase fluctuation is determined as a function of position in the pupil.

The pyramid sensor is a generalization of the classical Foucault test. A “pyramid” prism having four faces, is located at the focus (Ragazzoni 1996). The prism splits the focal plane into four quadrants, each of which is re-imaged to form a pupil image on a detector (Fig. 4). Differences in irradiance between the four images, as a function of position in the pupil, are proportional to the displacement of rays in the image plane. Thus, the components of the wavefront slope in the pupil can be recovered from irradiance differences between the pupil images. The subapertures of the pyramid sensor are defined by averaging or binning in the pupil images, which is done by software.

Saturation occurs when the irradiance at any location in any of the pupil images drops to zero. To increase the dynamic range of the sensor, modulation can be introduced by translating the prism transversely in the focal plane, much like moving the knife edge in a Foucault test. Typically, the prism vertex traces a circular path around the nominal position of the reference star image and the irradiance is integrated over the period of the motion. The amplitude of this modulation can be changed to control

the dynamic range of the sensor. Alternative non-dynamical sources of modulation, such as a diffusing screen (Ragazzoni et al. 2002b) have also been proposed. In addition, uncorrected atmospheric turbulence is a source of modulation, which increases the dynamic range of the sensor (Costa et al. 2003; Costa 2005).

Pyramid sensors benefit from the fact that when the AO loop is closed, the reference star is sharpened to essentially the diffraction limit of the full aperture (rather than that of a subaperture as in the Shack–Hartmann WFS). The modulation of the prism can then be reduced to increase the sensitivity. The improved performance of the pyramid sensor, compared to Shack–Hartmann, has been demonstrated both by analysis (e.g. Esposito and Riccardi 2001) and by observation (Peter et al. 2010). The improvement is found to be greatest for low-order modes, making pyramid sensors particularly attractive for high-contrast applications such as exoplanet imaging.

The curvature sensor is an elegant device that makes use of the fact that phase fluctuations develop into irradiance fluctuations during propagation. By multiplying Eq. (8) by  $\Psi^*$ , setting  $n = 0$ , substituting from Eq. (10), and collecting the imaginary terms we obtain the irradiance transport equation

$$-k \frac{\partial I}{\partial z} = I \nabla^2 \varphi + \nabla I \cdot \nabla \varphi. \quad (56)$$

The first term on the right-hand side of the equation corresponds to the focussing effect of wavefront curvature and the second corresponds to the lateral shift produced by a wavefront gradient. From this we see that dimensionless irradiance fluctuations  $\delta \ln I$  grow with propagation distance, in proportion to the wavefront curvature.

The irradiance fluctuations are maximal, and nonlinear, at any focus and change sign when passing through the focus. However, beyond a short distance from the focus, the linear approximation is valid. In the linear region, the difference in irradiance between two images recorded before and after the focus is proportional to the curvature of the wavefront in the corresponding position in the pupil. By integration, a map of the phase fluctuation across the pupil can be constructed (Roddiier and Roddiier 1988).

One can also determine the wavefront phase by interferometric techniques, and a variety of devices have been developed for this purpose. These include shearing interferometers (e.g. Sandler et al. 1994), amplitude splitting interferometers, and phase shifting interferometers (Wallace 2011). The shearing interferometer is most commonly used (see Welsh et al. 1995, for a comparison with the Shack–Hartmann sensor).

#### 4.3 Wavefront correction

Low-order Zernike modes can be corrected by a variety of techniques. Wavefront tilt and focus can be compensated by tilting or translating plane mirrors, or by translating lenses. However, good AO performance generally requires correction of tens or even hundreds of Zernike modes. This is accomplished by the use of deformable mirrors.

Most commonly used are piezoelectric mirrors, in which a thin glass face sheet, polished, aluminized and coated, is bonded to a two-dimensional stack of piezoelectric

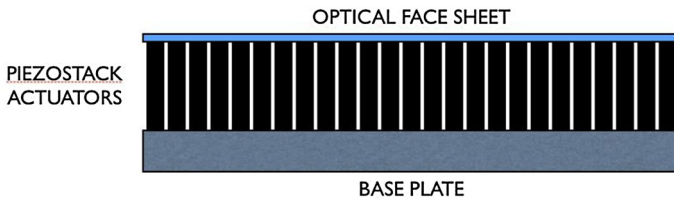


**Fig. 5** Piezoelectric deformable mirror structure. An array of stacked piezoelectric actuators is secured to a rigid base plate. The top surfaces of these actuators are bonded to a flexible glass face sheet. A reflective coating is deposited on the upper surface of this sheet. Voltages applied to the individual actuators cause the face sheet to flex, introducing phase shifts in the reflected light

actuators (Fig. 5). Forces applied by the actuators bend the glass, allowing control of the shape of the optical surface. Piezoelectric DMs have a typical inter-actuator spacing (pitch) of a few millimeters, and a stroke on the order of a micron. Devices with  $\sim 10^3$  actuators are now available, and devices with  $\sim 10^4$  actuators are under development.

Bimorph DMs employ a mirror bonded to a wafer of piezoelectric ceramic material. Voltages applied to electrodes imprinted on the ceramic produce bending of the mirror. To first-order, the resulting local curvature of the mirror surface is proportional to the applied voltage. These mirrors have been employed in several astronomical AO systems. They are particularly well suited to low-order AO systems using curvature sensors, which produce a signal that can be applied to the bimorph mirror with little processing.

MEMS (micro electro-mechanical systems) DMs consist of thousands of miniature mirrors or a face sheet with tiny actuators, fabricated on a silicon wafer (Gavel 2006). Mirror motion is produced by electrostatic forces, controlled by an integrated circuit. They are smaller than piezoelectric DMs and have much simpler drive requirements. The largest devices presently available have 4,096 actuators, with inter-actuator spacing on the order of 0.3 mm and a stroke of up to 3.5  $\mu\text{m}$ . While this stroke is not sufficient to provide full atmospheric correction over a large telescope aperture it can be extended by the use of “woofer–tweeter” combinations in which a low-order piezoelectric DM is used in conjunction with a MEMS DM (e.g. Perez et al. 2009). Further development of MEMS technology may overcome this stroke limitation (Fernández and Kubby 2010).

#### 4.4 AO control

Adaptive optics requires a control system that processes signals from the WFS and applies corrections to the DMs and tip-tilt mirrors. At the same time, large-amplitude low-frequency errors are converted to tracking corrections for the telescope drives. The input to the system is the aberrated wavefront phase, and the output is the AO corrected wavefront. Most AO systems employ closed-loop operation. The corrected wavefront is measured by the WFS and the required correction is computed and applied to the DM.

Control systems are characterized by transfer functions, which describe the frequency responses of combinations of elements of the system. Of particular importance

is the rejection transfer function, which characterizes the response to a disturbance, such as a fluctuation in the input wavefront phase. The characteristic time of the system is the time required to reduce a disturbance by a factor  $1/e$ . Naturally, this time must be short compared to the atmospheric coherence time, described by the Greenwood frequency  $f_G$  (Sect. 2.5). Typically,  $f_G$  is in the range 10–100 Hz. The characteristic frequency of AO control systems is normally much larger than this,  $\sim 10^3$  Hz, in order to reduce errors caused by control system lag.

The control system receives as inputs a large number of signals from the wavefront sensor(s), and provides outputs to drive the DM elements. For example, for a Shack-Hartmann WFS having  $n$  sub apertures, the signal consists of  $2n$  slope measurements  $\hat{s}_i$ , from which one must derive the wavefront phase  $\phi_j$  at  $m$  points in the pupil. The slopes are derivatives of the phase, which can be represented by a matrix equation  $s = A\phi$ , where  $A$  is a  $2n \times m$  “geometry” matrix. To determine the phase, this equation must be inverted. The presence of noise in the measured values complicates this since the formal inverse of  $A$  may contain large values that would amplify the noise. Instead, one determines a matrix  $B$ , the “reconstructor” such that  $\phi = Bs$  minimizes the error in the derived phase when noise is included. The reconstructor matrix depends on the statistical properties of the noise. Gaussian noise can be completely characterized by the noise covariance matrix  $C$ , whose elements are the variance and covariances of the noise in the input channels.

When applying the phase correction, one must take into account the electromechanical properties of the DM. A voltage applied to one actuator will also cause some motion of the surface at adjacent actuators. This is described by an “influence matrix”, whose elements are the response at pupil location  $i$  due to a unit signal applied to actuator  $j$ . The inverse, or pseudoinverse of this matrix is applied to undo the crosstalk.

## 5 Advanced techniques

A serious limitation of conventional SCAO results from angular anisoplanatism (Sect. 2.6). Light propagating to the telescope from a science target, located at an angle  $\theta$  from the reference star, follows a different path through the atmospheric turbulence. Because of this, the phase correction required differs from what is sensed using light from the reference star. This leads to a loss of performance that increases with angle.

We see from Eq. (49) that the phase error grows with angle from the reference star, reaching unity at the isoplanatic angle, with a corresponding reduction in the Strehl ratio by a factor of  $1/e$ . At typical astronomical sites,  $\theta_0 \sim 2-3$  arcsec at a wavelength of  $0.5 \mu\text{m}$  (Skidmore et al. 2009). Thus, for good AO performance, a bright reference star is needed within a few arcsec of every science target. Of course most targets do not have such a star nearby and therefore cannot be observed using classical AO. Thus, classical SCAO systems, using natural guide stars, have poor sky coverage.

### 5.1 Laser adaptive optics

In order to overcome the sky coverage limitation of classical AO, lasers can be employed to create artificial laser guide stars (LGS) in the atmosphere (Foy and

Labeyrie 1985; Thompson and Gardner 1987). The return flux can arise from Rayleigh, Mie and Raman scattering in the troposphere and resonant scattering from alkali metals in the mesosphere. In Rayleigh systems, e.g. Talbot et al. (2006), a laser beam is projected towards the target by a small launch telescope generally located behind the secondary mirror. As the beam propagates through the troposphere, Rayleigh scattering creates a line of illumination. To create a star-like source, a pulsed laser is used, and the WFS is range gated (electronically shuttered to admit photons arriving from a specified range). This creates a compact LGS at the desired range in the atmosphere, typically  $\sim 10$  km.

Sodium systems employ lasers tuned to the D<sub>2</sub> line of atomic sodium at a wavelength of 589 nm. This enables them to create LGS by resonant excitation of sodium atoms in the mesosphere at an altitude of approximately 90 km. The greater altitude of the sodium region provides more complete sampling of the atmospheric turbulence (due to the cone effect discussed in Sect. 5.2).

A common problem affecting LGS systems is tilt degeneracy. The tilt components of atmospheric turbulence cannot be sensed using a LGS. The reason for this is that when the laser travels upward through the atmosphere (the “uplink beam”) it is deflected by an angle that is equal and opposite to the deflection that occurs when the light returns to the telescope from the LGS (the “downlink beam”). Because of this, at least one natural guide star (NGS) is needed by a laser AO system. Similarly, for sodium systems, atmospheric focus is not well sensed because one does not normally know the precise range of the LGS. Thus focus information, at least at low temporal frequencies, must be obtained from a NGS. This limitation could be overcome using a pulsed laser system, in which the range can be determined by timing. However most sodium AO systems employ continuous wave (CW), laser systems, or quasi-CW pulsed lasers in which the repetition rate is much higher than the WFS readout frequency.

## 5.2 Tomography

A well-known problem affecting laser AO systems is the “cone effect”, also known as focus anisoplanatism (Tallon and Foy 1990). Because of the finite range of the LGS, light propagating back to the telescope is confined to the interior of a cone. In contrast, light from astronomical sources that reaches the telescope propagates within a cylinder. The region of the atmosphere outside the cone, but within the cylinder, affects the image of the target but is not sensed by the LGS and therefore cannot be corrected. The solution to this problem is atmospheric tomography (Fig. 6).

In a laser tomography adaptive optics (LTAO) system, multiple LGS are generated, either by multiple lasers or an optical system (an “asterism generator”) that splits the light from a single laser before directing it to the launch telescope. The light from each LGS in the asterism is directed to a separate WFS. This allows a complete sampling of the region of the atmosphere through which light from the science field propagates. Typically one employs a central LGS surrounded by four or five LGS equally spaced around a circle.

The wavefront phase errors sensed by all the WFS are combined to estimate the atmospheric propagation delays throughout the sampled volume, in a process of tomo-



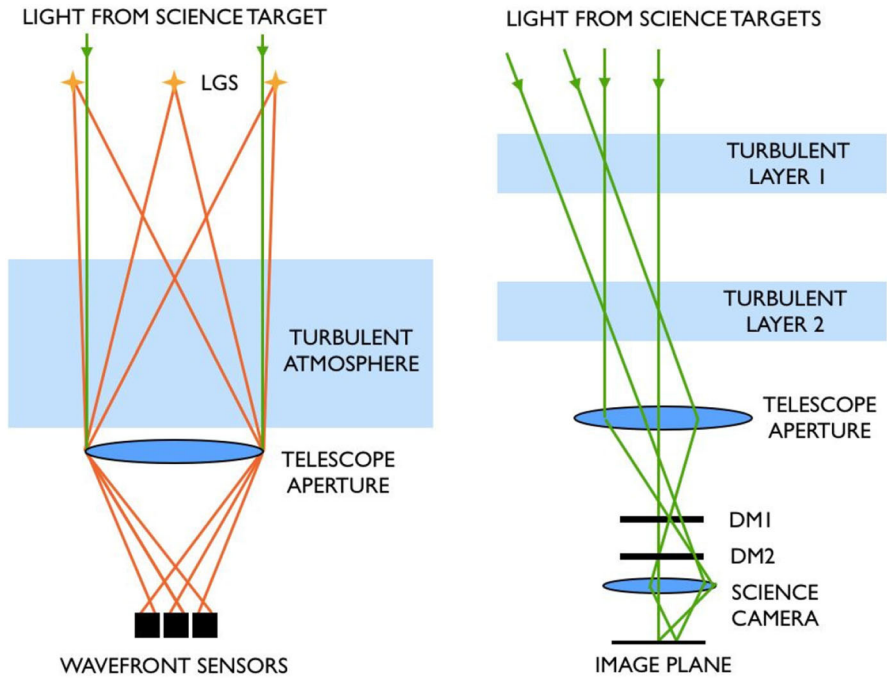


**Fig. 6** *Left panel* Atmospheric tomography. Light from a single LGS cannot probe the entire volume of the atmosphere that affects light from a distant science target (the cone effect). This problem is overcome by the use of multiple LGS, and an algorithm that uses signals from all the corresponding WFS to construct a model of the instantaneous index of refraction fluctuations throughout the volume. *Right panel* MCAO employs two (or more) DMs located optically conjugate to principle layers of turbulence. This allows the system to correct over a wider field of view, effectively increasing the isoplanatic angle (for simplicity, the change in direction of the light due to reflection by the DMs is not shown)

graphic reconstruction (Beckers 1988; Tallon and Foy 1990; Johnston and Welsh 1994; Ellerbroek 1994). In this process, the atmosphere is divided into a grid of cells that have horizontal dimension  $w \sim r_0$ , comparable to a subaperture, and a vertical extent  $\delta h \sim w/\theta$ , where  $\theta$  is the angular radius of the science field. The phase error induced by propagation through each cell forms a vector  $X$  of  $n$  unknown quantities to be determined. The set of observed wavefront phase measurements from all WFS form a vector  $\hat{Y}$  of  $m$  measured quantities. The atmospheric propagation is computed using geometrical optics. Diffraction can be neglected since the subaperture size is typically much larger than the Fresnel length. In this approximation the phase contributions from different atmospheric layers add linearly. Therefore, the predicted values  $Y$  of the wavefront phase measurements are given by a linear matrix equation

$$Y = GX, \quad (57)$$

where  $G$  is an  $m \times n$  matrix that describes the phase error accumulated by propagation through the volume from each LGS to each subaperture of the respective WFS. The

matrix  $G$  depends on the geometry of the asterism and wavefront sensors, and the resolution of the tomographic model.

Equation (57) is inverted to give the atmospheric phases  $X$  from the WFS data  $\hat{Y}$ . The measured values  $\hat{Y}$  differ from the predicted values  $Y$  because of noise and modelling limitations, so some form of regularization is needed. Minimum-variance techniques (e.g. Fusco et al. 2001; Tokovinin and Viard 2001; Ellerbroek 2005) compute a linear estimator  $E$  that minimizes the error  $|E\hat{Y} - X|^2$ .

Once  $X$  is known, the phase distortion can be computed for any direction in the science field and applied to one or more deformable mirrors. The measurements must be repeated continuously typically at a rate of  $\sim 1$  kHz, in order to follow the evolution of the turbulence.

In order to provide complete coverage of the atmospheric volume, the angular spacing between reference stars (either NGS or LGS) should be no greater than  $D/h$ , where  $h$  is the effective vertical extent of the turbulent atmosphere above the observatory, typically  $\sim 10$  km. This gives a maximum separation of  $\sim 3$  arcmin for an 8-m telescope. For a 100-m telescope, this separation increases to  $\sim 30$  arcmin. As will be discussed in Sect. 5.7, this may be large enough to provide reasonable sky coverage using natural stars alone. However, for at least the next generation of large telescopes, lasers will be required.

### 5.3 MCAO

The concept of multi-conjugate adaptive optics (MCAO: Dicke 1975; Beckers 1988, 1989) addresses the problem of angular anisoplanatism. By inserting additional deformable mirrors, conjugated to different heights in the atmosphere, anisoplanatism can be greatly reduced. The concept is most easily visualized by imagining that turbulence is concentrated in two thin layers, one at ground level and the other at a high altitude (Fig. 6). An SCAO system, conjugated to the ground layer, can correct the turbulence only for one line of sight. Other lines of sight pass through different high-altitude turbulence. Now add a second DM, optically conjugate to the high altitude layer. At the same time add one or more WFS, viewing different stars (NGS or LGS), so that the phase delays produced by the two layers can be distinguished. Now apply the correction needed for each layer to the appropriate DM. This effectively removes the atmospheric turbulence *for all lines of sight*, resulting in the elimination of anisoplanatism. Of course this idealized situation does not exist, as turbulence is distributed throughout the atmosphere (Fig. 1). To fully correct it would require an infinite number of DMs and WFSs. Nevertheless, great improvement can be achieved with only two or three DMs.

The first operational MCAO system, ESO's Multi-conjugate Adaptive-optics Demonstrator (MAD) employed two bimorph DMs and three Shack–Hartmann WFSs sensing natural stars (Marchetti et al. 2007; Bouy et al. 2008). The conjugate altitudes of the two DMs were 0 and 8.5 km above the telescope. Although the use of NGS resulted in limited sky coverage, this did not matter for a concept demonstrator. The results from MAD are impressive. Over a 1 arcmin field, the image FWHM in the Ks band was in the range 0.09–0.12 arcsec with Strehl ratios in the range 0.1–0.25 (Bouy et al. 2008).

The first laser MCAO system is operating at the Gemini South observatory ([Neichel 2012](#)). The Gemini Observatory MCAO System (GEMS) employs three DMs and an asterism of 5 LGS. It is expected to achieve Strehl ratios in the range 0.45–0.80 in the 1–2  $\mu\text{m}$  wavelength range, with relative Strehl variations of less than 6 % across a 1-arcmin field of view. Initial tests have already achieved Strehl ratios  $>0.4$ , with the expected uniformity. MCAO systems are integral to the next generation of extremely-large telescopes (ELTs), with both the European ELT (E-ELT) and the Thirty Meter Telescope (TMT) intending to provide MCAO as a facility capability ([Diolaiti et al. 2010](#); [Ellerbroek et al. 2010](#)).

#### 5.4 MOAO

Multi-object adaptive optics (MOAO) is a new concept to provide AO correction for designated targets within a wide field of view. Each target is imaged by a separate optical system, which employs its own dedicated DM, feeding an imaging camera or integral field spectrometer (IFU). These “science channels” can patrol the field of view, being robotically positioned on targets of interest. The DM correction required for each target is computed from a tomographic reconstruction of the atmosphere.

Unlike other AO systems, MOAO uses open-loop control. There is no feedback provided to the control system from any image corrected by the individual DMs in the science channels (although additional DMs might be used to correct the wavefronts of the guide stars). This places greater requirements on the predictability and linearity of the deformable mirror. Because of this, it is expected that the delivered Strehl ratio may not be as high as that achievable by MCAO. However, the field of view of MOAO can be several arcmin, and the achievable correction is well suited to IFU spectroscopy.

MOAO systems are being planned by both the E-ELT and TMT projects. These are very ambitious systems, which are expected to be brought online within the first decade of telescope operation.

#### 5.5 GLAO

An interesting new concept is ground-layer adaptive optics (GLAO: [Angel and Lloyd-Hart 2000](#); [Rigaut 2002](#)). Its principle is to correct only the strong low-level turbulence and not the high atmospheric layers. This differs from SCAO, which corrects all layers but only in a single direction. By correcting only the ground layer, one can achieve improved image quality (compared to natural seeing) over a wide field of view. A single DM is placed optically conjugate to the ground layer, resulting in a large isoplanatic angle for this layer. The images are still blurred by the high atmospheric layers, so this technique generally does not achieve the diffraction limit. Instead, GLAO can be viewed as a means of improving the seeing, by eliminating the contribution from the ground layer. This can lead to substantial gains in efficiency for wide-field seeing-limited multi-object spectroscopy. A rough estimate can be made by noting that in the Cerro Pachón atmospheric model, the ground layer contributes 64 % of

the total turbulence integral. Since the image FWHM  $\varepsilon \propto r_0^{-1} \propto J^{3/5}$ , complete elimination of the ground layer should typically decrease the FWHM by a factor of  $0.36^{3/5} = 0.54$  and increase the central intensity of the PSF by a factor of  $0.54^{-2} = 3.4$ .

GLAO is implemented by means of multiple reference stars, either NGS or LGS can be used, and an equal number of WFS. It is not necessary to do a full tomographic reconstruction. Instead, the mean wavefront phase is determined from all the WFS and the result is applied to a single DM, conjugated to the ground layer. This provides the best average correction over the region of sky sampled by the guide stars.

A concept-demonstrator GLAO system has been operated at the Multiple Mirror Telescope (MMT, [Bendek et al. 2011](#)). It employs five Rayleigh lasers, that are range-gated and dynamically refocussed, to sense the turbulence in five directions. The wavefront correction is applied to the MMTs 336-actuator adaptive secondary mirror. A GLAO system employing 6 Rayleigh lasers, range gated to a distance of  $\sim 12$  km, and providing a 4-arcmin field of view, is being developed for the Large Binocular Telescope (LBT, [Hart et al. 2011](#)). GLAO will be a primary capability for both the E-ELT and the Giant Magellan Telescope (GMT, [Johns et al. 2012](#)).

## 5.6 ExAO

Perhaps the most challenging application of AO is the field of high-contrast imaging. The aim here is to not only achieve diffraction-limited resolution but also to suppress light diffracted out of the PSF by atmospheric turbulence and imperfections in the telescope optics, to a very high degree. This is necessary in order to detect planets that are normally hidden within the glare of their parent stars. Diffracted and scattered light from the star can be suppressed by means of coronagraphy, in which judiciously-placed occulting masks or interferometric systems block or cancel much of the starlight while transmitting light from the planet. However, this works only to the extent that the incident light is coherent. Therefore an adaptive optics system is needed to restore the coherence that is lost due to atmospheric turbulence. Typically, a fraction  $1 - S$  of the light remains uncorrected, so the AO system must have a very high Strehl ratio.

Extreme adaptive optics (ExAO) typically employs a high-order SCAO system that uses the light from the host star for wavefront sensing. The AO-corrected image is then passed to a coronagraphic imager or nulling interferometer. Fundamental limits to the achievable contrast come from photon noise, speckle noise, and chromatic effects related to the differences between the wavelengths employed for the science observation and the AO system ([Guyon 2005](#)). Chromatic effects within the coronagraph can be reduced by means of chromatic phase masks, which have already been successfully tested ([Mawet et al. 2005](#)). In practice, systems are primarily limited by uncorrected speckle noise ([Racine et al. 1999](#)).

The achievable contrast can be further improved by post-processing data analysis techniques such as angular differential imaging (ADI, [Marois et al. 2006](#)) or simultaneous spectral differential imaging (SSDI, [Racine et al. 1999](#); [Lafrenière et al. 2007](#)) in

**Table 4** Adaptive optics techniques

Technique	Main features	Implementation
SCAO	High Strehl on axis, limited sky coverage	Single NGS
LTAO	High Strehl on axis, good sky coverage	Multiple LGS, 1 DM
MCAO	High Strehl, large FOV, uniform PSF	Multiple LGS, 2+ DMs
MOAO	Multiple well-corrected fields	Multiple LGS, individual DMs
GLAO	Partial correction over very-large FOV	Multiple NGS or LGS, 1 DM
ExAO	High contrast	Single bright NGS

which the quasi-static pattern of speckles produced by imperfections in the telescope optics is reconstructed and subtracted from a series of images taken at different pupil orientations or wavelengths. Recently, improved data processing methods based on principal component analysis have been proposed (Soummer et al. 2012; Amara and Quanz 2012) and are now being tested on the sky.

Current AO systems have already produced the first images of exoplanetary systems (Chauvin et al. 2005; Marois et al. 2008). And, sophisticated ExAO systems such as the Gemini Planet Imager (Macintosh et al. 2006) and SPHERE at ESO's Very Large Telescope (VLT, Dohlen et al. 2006) are being built. The next generation ELTs will all feature advanced ExAO systems.

### 5.7 Layer-oriented AO

An alternative approach to adaptive optics has been proposed by Ragazzoni and collaborators Ragazzoni (1999), Ragazzoni et al. (2000, 2002a). Layer-oriented adaptive optics (LOAO) offers the prospect of wide field AO correction without any laser guide stars. The essential difference between LOAO and conventional star-oriented MCAO is that LOAO senses many stars simultaneously on a single WFS, which is optically conjugate to a particular altitude and drives a single DM conjugated to the same altitude. In the LOAO scheme there are many such WFS–DM pairs, each conjugated to a different altitude or atmospheric layer. Since the WFS signal is derived from the light of many stars, these stars can be fainter than those required for conventional AO. With a large enough telescope aperture, natural stars may suffice to give wide, or even complete, sky coverage. LOAO has yet to be demonstrated, although a prototype LO sensor was tested with the MAD AO system at ESO with promising results (Vernet et al. 2005; Arcidiacono et al. 2007).

### 5.8 Summary of techniques

The various AO techniques described in this section all have advantages and disadvantages. The choice of technique is largely driven by the nature of the scientific programs that will be conducted with the system. Table 4 summarizes the principle advantages, disadvantages and implementation of each AO technique.

## 6 AO performance

Adaptive optics can provide gains in both resolution and sensitivity. However, the AO-corrected image is not perfect. Variations in the Strehl ratio, and intensity distribution in the PSF, occur both in time and position in the field. This leads to difficulties in photometric and astrometric analysis of AO images. Improvements in both the theoretical understanding, and the technology are helping to address these issues.

### 6.1 Image quality and telescope sensitivity

No AO system provides complete correction of the wavefront. Residual phase errors remain over the full spectrum of atmospheric spatial frequencies. These fluctuations diffract light into a broad “halo” that surrounds a compact image core. In long-exposure images, the core resembles the diffraction-limited PSF  $I_0$  and contains a fraction  $S$  of the light equal to the Strehl ratio. The remaining light is contained in the halo, which has a distribution similar to the PSF produced by atmospheric seeing,  $I_A$ . Thus,

$$I = SI_0 + (1 - S)I_A. \quad (58)$$

The characteristic width of  $I_A$  is greater than that of  $I_0$  by the ratio  $D/r_0$ , typically  $\sim 20$  for an 8-m telescope at near-infrared wavelengths. Thus, even for Strehl ratios as low as a few percent, the peak intensity of the halo is much lower than that of the core. Generally, the second term in Eq. (58) is neglected, although it can be important in crowded fields and when precision photometry is needed. It is also important when observing diffuse objects such as galaxies, and when observing faint sources near bright ones (for example, exoplanets and the environments of active galactic nuclei).

For observations of a faint unresolved target, the integration time required to reach a given signal-to-noise ratio is proportional to the product of background intensity  $I_B$ , telescope area and PSF area, and inversely proportional to the square of the flux contained within the PSF. Defining the sensitivity  $\mathcal{S}$  as the reciprocal of the required integration time, we see that

$$\mathcal{S} \propto \eta S^2 D^4 / I_B, \quad (59)$$

where  $\eta$  is the product of telescope and AO system throughput and detector quantum efficiency. This shows that very substantial gains in sensitivity are possible for large telescopes employing AO (the so-called  $D^4$  advantage). This, and the high gain in angular resolution, are the primary motivating factors for AO on large telescopes.

In long-exposure images, the PSF of Eq. (58) is further degraded by residual image motion, which can result from uncorrected atmospheric distortion, refraction, wind shake, vibrations and tracking errors. In an SCAO system, atmospheric tilt fluctuations increase with distance from the reference star (tilt anisoplanatism). Also, the residual tilt components are anisotropic, the longitudinal component (in the direction of the reference star) being greater than the transverse component by a factor of  $\sqrt{3/2}$ . As a result, the images become elongated.

With MCAO the situation is more complex. The AO system tries to keep the locations of the reference stars (NGS) constant, thereby “pinning” the field at those positions. Tilt anisoplanatism creates fluctuating field distortion that increases with distance from the reference stars. This results in image smearing and elongation, which varies with location in a complex, but predictable, manner. Even so, this is a significant improvement over SCAO, where the field is pinned only at a single point—the location of the reference star.

## 6.2 AO system performance

The performance of an AO system can be assessed in many ways. The most straightforward is the delivered Strehl ratio, or RMS wavefront error, for an agreed observational configuration and atmospheric conditions. This has a direct impact on resolution and sensitivity, particularly for imaging observations. In the case of spectroscopy, a better metric might be the delivered energy within a specified area, such as a slit size or IFU spatial pixel size. Often, the field of view over which this image quality is delivered is important. The performance usually depends on the number, magnitudes and positions of one or more NGS. The probability of finding suitable stars depends on galactic latitude.

Sky coverage is determined by the availability of suitable natural guide stars. Requirements for sky coverage normally assume a random location, or alternatively the worst case, the galactic pole. Median atmospheric conditions are perhaps the best assumption, but one is generally also interested in the performance under good conditions, such as the best 10th or 25th percentile. Of course it is best to consider specific scientific programs when possible and examine the fields directly to see what can be observed successfully with a given AO system.

Near the diffraction limit, Strehl ratio is determined by the RMS phase error averaged over the pupil (Eq. 55). In order to predict the performance of any AO system, one must consider all the factors contributing to the wavefront error. Some of the main contributions are:

- fitting error: the error resulting from the finite number of DM actuators and/or WFS subapertures;
- tomographic error: the error resulting from imperfect 3-d modelling of the atmospheric turbulence;
- servo lag error: the error resulting from the finite response time of the AO control system;
- wavefront sensor noise: the error resulting from photon noise and detector read noise;
- non-common-path errors: errors that are not sensed by the AO system, such as aberrations in the science channel after the beamsplitter that sends light to the WFS;
- chromatic errors: errors resulting from differences in wavelength between the WFS wavelength and the science wavelength (e.g. differential atmospheric refraction).

In AO system design, all these sources of error, and others, are considered and apportioned in an error budget in order to maximize the performance. This is a complex



process since many of these errors are coupled. For example, increasing the integration time for the WFS will reduce the error due to photon noise, and possibly detector read noise, but will increase the servo-lag error. If one uses brighter NGS, this will reduce photon noise, but may reduce sky coverage.

At the same time, the flexibility provided by the many design parameters allows the AO system to be tuned to some degree, to better suit particular observing programs or the atmospheric conditions. For example in an MCAO system, spreading the LGS asterism over a wider angle should increase the field of view over which reasonable AO correction can be provided. But at the same time, it will likely lower the average Strehl ratio.

### 6.3 Photometric and astrometric accuracy

AO dramatically improves image resolution and detection limits. It reduces confusion in crowded fields, making possible science programs that would not be feasible in natural seeing. But, at the same time AO introduces new complications for photometric and astrometric analysis. The primary issue is variation of the PSF within the field of view. Depending on the type of AO system, and the nature of the observations, PSF variations can be very substantial. Even with MCAO systems, Strehl ratio variations of tens of percent are typical. Astronomical data analysis software must be able to handle this. Fortunately, algorithms that can accommodate a variable PSF already exist, since all telescope images suffer from this problem to some degree. With AO, the PSF variations are greater, so more care is needed.

For photometry of stellar images, the best results possible come from the technique of PSF fitting, which can be shown to be optimal in the sense of providing the smallest photometric error in the presence of uniform additive Gaussian noise (King 1983). Programs such as DAOPHOT (Stetson 1987), which employs linear optimization of PSF fits to the stellar images, can accommodate a degree of PSF variation. For any such technique a good knowledge of the PSF is essential.

It follows that an important aspect of future AO systems will be PSF prediction. By recording the signals produced by all WFS during an integration, and combining this with a knowledge of the guide star geometry AO system configuration, and atmospheric parameters, it is possible to reconstruct the form of the AO-corrected PSF anywhere in the field (Véran 1997).

An important new capability provided by AO is precision astrometry. Already, an accuracy on the order  $\sim 200 \mu\text{as}$  for relative astrometry is achieved by SCAO systems on 8–10 m telescopes (Ghez 2008) at the Galactic centre. The ELT AO systems will benefit from a smaller FWHM and higher sensitivity (resulting in more detected stars). In addition, MCAO systems allow a wider field of view, better PSF uniformity, and reduce the atmospheric distortion over the field (Meyer et al. 2011). The E-ELT and TMT projects have set targets in the 30–50  $\mu\text{as}$  range, with an eventual goal of 10  $\mu\text{as}$ . Such precision would open up new scientific frontiers such as black hole dynamical studies in local galaxies, 3-dimensional stellar kinematics, astrometric microlensing, astrometric planet detection and many other programs. The achievement of high astrometric precision is therefore a high priority for these telescopes and their AO systems.



Achieving such precision is challenging, requiring attention to many details. Effects such as atmospheric dispersion, high-order field distortion, PSF variations, tracking errors, mechanical flexure and bearing tolerances, calibration mask errors, etc., all become significant (Trippe et al. 2010). Moreover, many of these effects are coupled. For example a tracking error that produces an image elongation of  $\sim 1$  mas, when combined with a variation in atmospheric transparency during the integration, can lead to differential astrometric errors of as much as  $100 \mu\text{as}$ .

#### 6.4 Challenges of LGS systems

An obvious issue with the use of lasers is light pollution. Many sites, such as Mauna Kea, are home to several major observatories. One does not want a laser, propagated by any observatory to contaminate the observations of another telescope. This requires planning and coordination between observatories.

More subtle is the effect of contamination by multiple laser beams being launched by the same telescope, as required by MCAO, MOAO or GLAO systems. Rayleigh scattering from the beams can contaminate the subapertures that they cross. The result is a loss of performance due to additional background noise in the affected subapertures, referred to as “fratricide” (Wang et al. 2010). Fratricide primarily affects telescopes employing centre-launched lasers. Side-launched lasers reduce fratricide as they do not need to cross in front of the telescope aperture in order to form the perimeter stars in the LGS asterism.

Related to this is scattering within cloud layers. Thin cirrus clouds occur frequently at many astronomical sites. These doubly attenuate LGS since both the uplink and downlink beams are affected. In addition, multiple scattering of laser photons within a cloud can result in a substantial fraction of light being scattered back towards the telescope. Thus, a glow surrounds the laser beam as it enters a cloud. This is more of an issue with tomographic systems due to the number of beams and high laser power entering the cloud. Preliminary calculations suggest that it should be possible to operate these systems when the total optical depth of cirrus clouds is less than a few tenths.

For sodium laser AO systems, additional complications arise from the structure and variability of the mesospheric sodium region. This region of the atmosphere is a dynamic one, affected by gravity (buoyancy) waves, wind shear, tides and chemistry. Sodium is found with greatest concentration between altitudes of approximately 80–110 km. It is generated by meteoric deposition and removed by chemical reactions (Plane 2003). Within this region the density and structure can change dramatically on timescales of minutes to hours. Substructure occurs within the region, primarily in the form of near-horizontal layers, which form, migrate, and dissipate. High-resolution lidar imaging reveals coherent oscillations, instability and turbulence within the region (Pfrommer et al. 2009). Sporadic layers, containing high concentrations of sodium, can appear within minutes.

Because of the finite thickness of the sodium region, LGS are actually cylinders of light. For a large telescope, different parts of the pupil see the LGS slightly obliquely, creating image elongation that varies with subaperture. Thus, the images within each cell of a Shack–Hartmann sensor are small streaks, containing substructure reflecting

the vertical structure of the sodium density. As this changes, the location of the centroid of the Shack-Hartmann images changes, creating errors in the derived wavefront phase.

The magnitude of this effect clearly grows linearly with telescope aperture, and is a significant source of error in ELT AO systems. A number of techniques are being explored which address this problem, including matched filtering, thresholding and temporal filtering (Thomas et al. 2008; Lardière et al. 2010).

A related problem occurs due to variations in the mean sodium altitude, which affects the range of the LGS. A change in range produces a change in wavefront curvature, which LGS WFS interprets as a focus error. This error is substantial and grows as the square of the telescope diameter (Davis et al. 2006). For a 30 m aperture, a 1 m variation in altitude results in 4 nm of rms wavefront error. Because of this, LGS cannot be relied upon for curvature information, at least at low temporal frequencies, so this must come from NGS. But at high temporal frequency photon noise dominates the NGS signal, so LGS curvature information must be blended with the NGS signal for best results. Fluctuations in the sodium mean altitude are also expected to occur spatially, thus different LGS within an asterism will have different, and unpredictable, range fluctuations (Pfrommer and Hickson 2010). Future MCAO and MOAO systems will need to be designed in a way that mitigates these effects.

## 7 Conclusions

In the six decades since the concept of adaptive optics was first introduced, tremendous advances have been made, not just in the technology, but also in theoretical understanding and the development of advanced AO concepts and modes. These advances are made possible by the collaborative work of scientists and engineers covering a broad range of disciplines, including mathematics, theoretical physics, atmospheric physics, optics, mechanical, thermal and electronic engineering, control theory, computer and software engineering.

Adaptive optics systems are now standard at most major observatories and will be central to the next generation of ELTs. The number of papers reporting results from AO observations is increasing exponentially. AO observing time may soon match, or even exceed that of seeing-limited observations. New concepts such as MCAO, GLAO and ExOA, now coming on line, will greatly expand the scientific capabilities of astronomical facilities. Advanced techniques such as MOAO, LOAO, and perhaps others not yet imagined, offer promising directions for the future.

**Acknowledgments** I am indebted to many colleagues who provided insights into different aspects of this subject, but particularly to Jacques Beckers, Brent Ellerbroek, Marc Sarazin and Andrei Tokovinin. I am grateful to Jean Surdej for his encouragement, and to Andreas Quirrenback whose comments improved the manuscript. Part of this work was completed during sabbatical visits to the European Southern Observatory and the Université de Liège. I thank both institutes for their hospitality. Financial support was provided by the Natural Sciences and Engineering Research Council of Canada.

## References

- Amara A, Quanz SP (2012) PYNPOINT: an image processing package for finding exoplanets. *Mon Not R Astron Soc* 427:948–955

- Andrews LC (2004) Field guide to atmospheric optics. Society of Photo-Optical Instrumentation Engineers, Bellingham
- Andrews LC, Phillips RL (2005) Laser beam propagation through random media. Society of Photo-Optical Instrumentation Engineers, Bellingham
- Angel R, Lloyd-Hart M (2000) Atmospheric tomography with Rayleigh laser beacons for correction of wide fields and 30 m class telescopes. *Proc Soc Photo Opt Instr Eng* 4007:270–276
- Arcidiacono C, Lombini M, Farinato J, Ragazzoni R (2007) Toward the first light of the layer oriented wavefront sensor for MAD. *Mem S A It* 78:708–711
- Babcock HW (1953) The possibility of compensating astronomical seeing. *Publ Astron Soc Pac* 65:229–236
- Beckers JM (1988) Increasing the size of the isoplanatic patch with multiconjugate adaptive optics. In: Ulrich M-H (ed) *Proceedings of the ESO conference on very large telescopes and their instrumentation*. European Southern Observatory, Garching, pp 693–703
- Beckers JM (1989) Detailed compensation of atmospheric seeing using multiconjugate adaptive optics. *Proc Soc Photo Opt Instr Eng* 1114:215–217
- Beckers JM (1993a) Adaptive optics for astronomy: principles, performance, and applications. *Ann Rev Astron Astrophys* 31:13–62
- Beckers JM (1993b) On the relation between scintillation and seeing observations of extended objects. *Sol Phys* 145:399–402
- Bendek EA, Hart M, Powell KB, Vaitheeswaran V, McCarthy D, Kulesa C (2011) Latest GLAO results and advancements in laser tomography implementation at the 6.5 m MMT telescope. *Proc Soc Photo Opt Instr Eng* 8149:814907–814907-11
- Berdja A (2010) On the DIMM interpretation of non-Kolmogorov turbulence in the atmospheric surface layer. *Mon Not R Astron Soc* 409:722–726
- Bouy H, Kolb J, Marchetti E, Martin EL, Huélamo N, Barrado Y, Navascués D (2008) Multi-conjugate adaptive optics images of the Trapezium cluster. *Astron Astrophys* 477:681–690
- Businger S, Cherubini T (2011) Seeing clearly: the impact of atmospheric turbulence on the propagation of extraterrestrial radiation. Virtualbookworm.com Publishing, College Station
- Chauvin G, Lagrange A-M, Dumas C, Zukerman B, Mouillet D, Song I, Beuzit J-L, Lowrance P (2005) Giant planet companion to 2MASSW J1207334-393254. *Astron Astrophys* 438:L25–L28
- Clénét Y, Conan J-M, Fusco T, Rousset G (eds) (2010) 1st AO4ELT conference—adaptive optics for extremely large telescopes. EDP Sciences. <http://ao4elt.edpsciences.org>
- Costa J (2005) Modulation effect of the atmosphere in a pyramid wave-front sensor. *Appl Opt* 44:60–66
- Costa J, Ragazzoni R, Ghedina A, Carillet M, Verinaud C, Feldt M, Esposito S, Puga E, Farinato J (2003) Is there need of any modulation in the pyramid wavefront sensor? *Proc Soc Photo Opt Instr Eng* 4839:288–298
- Davies R, Kasper M (2012) Adaptive optics for astronomy. *Ann Rev Astron Astrophys* 50:305–351
- Davis D, Hickson P, Herriot G, She C-Y (2006) Temporal variability of the telluric sodium layer. *Opt Lett* 31:3369–3371
- Dicke RH (1975) Phase-contrast detection of telescope seeing errors and their correction. *Astrophys J* 198:605–615
- Diolaiti E, Conan J-M, Foppiani I et al (2010) Conceptual design and performance of the multiconjugate adaptive optics module for the European Extremely Large Telescope. *Proc Soc Photo Opt Instr Eng* 7736:77360R
- Dohlan K et al. (2006) SPHERE: a planet finder instrument for the VLT. *Proc Soc Photo Opt Instr Eng* 6269:62690Q–62690Q-12
- Duffner RW (2009) The adaptive optics revolution: a history. University of New Mexico Press, Albuquerque
- Ellerbroek BL (1994) First-order performance evaluation of adaptive-optics systems for atmospheric turbulence compensation in extended field-of-view astronomical telescopes. *J Opt Soc Am A* 11:783–805
- Ellerbroek BL (2005) Linear systems modelling of adaptive optics in the spatial-frequency domain. *J Opt Soc Am A* 22:310–322
- Ellerbroek B, Adkins S, Andersen D et al (2010) First light adaptive optics systems and components for the Thirty Meter Telescope. *Proc Soc Photo Opt Instr Eng* 7736:773604
- Esposito S, Riccardi A (2001) Pyramid wavefront sensor behavior in partial correction adaptive optic systems. *Astron Astrophys* 369:L9–L12
- Esposito S, Fini L (eds) (2013) Third AO4ELT conference—adaptive optics for extremely large telescopes. <http://ao4elt3.arcetri.astro.it>

- Fernández B, Kubby J (2010) High-aspect-ratio microelectromechanical systems deformable mirrors for adaptive optics. *J Micro/Nanolitho MEMSMOEMS* 9:041105
- Foy R, Labeyrie A (1985) *Astron Astrophys* 152:L29–L31
- Fried DL (1966) Optical resolution through a randomly inhomogeneous medium for very long and very short exposures. *J Opt Soc Am* 10:1372–1379
- Fusco T, Conan JM, Rousset G, Mugnier LM, Michau V (2001) Optimal wave-front reconstruction strategies for multiconjugate adaptive optics. *J Opt Soc Am A* 18:2527–2538
- Gavel D (2006) MEMS for the next generation of giant astronomical telescopes. *Proc Soc Photo Opt Instr Eng* 6113:43–47
- Ghez AM et al (2008) Measuring distance and properties of the Milky Way's central supermassive black hole with stellar orbits. *Astrophys J* 689:1044–1062
- Goodman JW (1985) *Statistical optics*. Wiley, New York
- Goodwin M, Jenkins C, Lambert A (2007) Improved detection of atmospheric turbulence with SLODAR. *Opt Express* 15:14844–14860
- Greenwood DP (1977) Bandwidth specification for adaptive optics systems. *J Opt Soc Am* 67:390–393
- Guyon O (2005) Limits of adaptive optics for high-contrast imaging. *Astrophys J* 629:592–614
- Hagelin S, Masciadri E, Lascaux F (2011) Optical turbulence simulations at Mt Graham using the Meso-NH model. *Mon Not R Astron Soc* 412:2695–2706
- Hardy JW (1998) *Adaptive optics for astronomical telescopes*. Oxford University Press, Oxford
- Hickson P, Lanzetta K (2004) Measuring atmospheric turbulence with a lunar scintillometer array. *Publ Astron Soc Pac* 116:1143–1152
- Hart M, Rabien S, Busoni L et al (2011) Status report on the Large Binocular Telescopes ARGOS ground-layer AO system. *Proc Soc Photo Opt Instr Eng* 8149:81490J–81490J-11
- Hickson P, Carlberg R, Gagne R, Pfrommer T, Racine R, Schoeck M, Steinbring E, Travouillon T (2010) Boundary-layer seeing measurements in the Canadian High Arctic. *Proc Soc Photo Opt Instr Eng* 7733:77331R–77331R-11
- Hill R et al (2006) Site testing for the Advanced Technology Solar Telescope. *Proc Soc Photo Opt Instr Eng* 6267:62671T
- Hufnagel RE, Stanley NR (1964) Modulation transfer function associated. *J Opt Soc Am* 54:52–60
- Johns M, McCarthy P, Raybould K, Bouchez A, Farahani A, Filgueira J, Jacoby G, Shectman S, Sheehan M (2012) Giant Magellan Telescope: overview. *Proc Soc Photo Opt Instr Eng* 8444:84441H
- Johnston DC, Welsh BM (1994) Analysis of multiconjugate adaptive optics. *J Opt Soc Am A* 11:394–408
- Kibblewhite E, Wild W (2006) *Adaptive optics*. Wiley-Interscience, Hoboken
- King IR (1983) Accuracy of measurement of star images on a pixel array. *Publ Astron Soc Pac* 95:163–168
- Kolmogorov AN (1941) On degeneration of isotropic turbulence in an incompressible viscous liquid. *Comptes Rendus (Doklady) de l'Academie des Sciences de l'URSS* 31:538–540 [Improving the speckle noise attenuation of simultaneous spectral differential imaging with a focal plane holographic diffuser. *Ap J* 661:1208–1217]
- Kornilov V, Tokovinin A, Voziakova O, Zaitsev A, Shatsky N, Potanin S, Sarazin M (2003) MASS: a monitor of the vertical turbulence distribution. *Proc Soc Photo Opt Instr Eng* 4839:837–845
- Kornilov V, Tokovinin A, Shatsky N, Voziakova O, Potatin S, Safonov B (2007) Combined MASS-DIMM instrument for atmospheric turbulence studies. *Mon Not R Astron Soc* 383:1268–1278
- Lafrenière D, Doyon R, Nadeau D, Artigau E, Marois C, Beaulieu M (2007) Improving the speckle noise attenuation of simultaneous spectral differential imaging with a focal plane holographic diffuser. *Astrophys J* 661:1208–1217
- Lardièrre O, Conan R, Clare R, Bradley C, Hubin N (2010) Performance comparison of centroiding algorithms for laser guide star wavefront sensing with extremely large telescopes. *Appl Opt* 49:G78–G94
- Lombardi G et al (2010) Surface layer characterization at Paranal Observatory. *Proc Soc Photo Opt Instr Eng* 7733:77334D–77334D-13
- Lukin VP (1996) *Atmospheric adaptive optics*. Society of Photo-Optical Instrumentation Engineers, Bellingham
- Macintosh B et al (2006) The Gemini Planet Imager. *Proc Soc Photo Opt Instr Eng* 6272:62720L
- Mandel L, Wolf E (1995) *Optical coherence and quantum optics*. Cambridge University Press, Cambridge
- Marchetti E, Brast R, Delabre B et al (2007) On-sky testing of the multi-conjugate adaptive optics demonstrator. *Messenger* 129:8–13
- Maréchal A (1947) Étude des effets combinés de la diffraction et des aberrations géométriques sur l'image d'un point lumineux. *Rev Opt* 26:257–277

- Marois C, Larfenière D, Doyon R, Macintosh B, Nadeau D (2006) Angular differential imaging: a powerful high-contrast imaging technique. *Astrophys J* 641:556–564
- Marois C et al (2008) Direct imaging of multiple planets orbiting the star HR 8799. *Science* 322:1348–1352
- Martin F, Tokovinin A, Agabi A, Borgnino J, Ziad A (1994) G.S.M.: a Grating Scale Monitor for atmospheric turbulence measurements. I. The instrument and first results of angle of arrival measurements. *Astron Astrophys Suppl* 108:173–180
- Mawet D, Riaud P, Absil O, Surdej J (2005) Annular groove phase mask coronagraph. *Astrophys J* 633:1191–1200
- Meyer E, Kürster M, Arcidiacono C, Ragazzoni R, Rix H-W (2011) Astrometry with the MCAO instrument MAD. An analysis of single-epoch data obtained in the layer-oriented mode. *Astron Astrophys* 532:A16
- Neichel B et al. (2012) Science readiness of the Gemini MCAO System: GEMS. *Proc Soc Photo Opt Instr Eng* 8447:84474Q–84474Q-24
- Noll RJ (1976) Zernike polynomials and atmospheric turbulence. *J Opt Soc Am* 66:207–211
- Obukhov AM (1941a) On the distribution of energy in the spectrum of turbulent flow. *Dokl Akad Nauk SSSR* 32:22–24
- Obukhov AM (1941b) *Izv Akad Nauk SSSR Ser Geograf Geofiz* 13:58
- Perez JJ, Toussaint GJ, Schmidt JD (2009) Adaptive control of woofer–tweeter adaptive optics. *Proc Soc Photo Opt Instr Eng* 7466:74660B. doi:[10.1117/12.824450](https://doi.org/10.1117/12.824450)
- Peter D, Feldt M, Henning T, Hippler S, Aceituno S, Montoya S, Costa J, Dorner B (2010) Exploring the on-sky performance of the worlds first near-infrared pyramid wavefront sensor. *Publ Astron Soc Pac* 122:63–70
- Pfrommer T, Hickson P, She C-Y (2009) A large-aperture sodium fluorescence lidar with very high resolution for mesopause dynamics and adaptive optics studies. *Geophys Res Lett* 36:L15831
- Pfrommer T, Hickson P (2010) High-resolution lidar observations of mesospheric sodium and implications for adaptive optics. *J Opt Soc Am A* 27:A97–A105
- Plane JMC (2003) Atmospheric chemistry of meteoric metals. *Chem Rev* 103:4963–4984
- Racine R, Walker GAH, Nadeau D, Doyon R, Marois C (1999) Speckle noise and the detection of faint companions. *Publ Astron Soc Pac* 111:587–594
- Ragazzoni R (1996) Pupil plane wavefront sensing with an oscillating prism. *J Mod Opt* 43:289–293
- Ragazzoni R (1999) *Astron Astrophys Suppl* 136:205–209
- Ragazzoni R, Farinato J, Marchetti E (2000) Adaptive optics for 100-m-class telescopes: new challenges require new solutions. *Proc Soc Photo Opt Instr Eng* 4007:1076–1087
- Ragazzoni R, Diolaiti E, Farinato J, Fedrigo E, Marchetti E, Tordi M, Kirkman D (2002a) Multiple field of view layer-oriented adaptive optics. *Astron Astrophys* 396:731–744
- Ragazzoni R, Diolaiti E, Vernet E (2002b) A pyramid wavefront sensor with no dynamic modulation. *Opt Commun* 208:51–60
- Richardson LF (1922) *Weather prediction by numerical process*. Cambridge University Press, Cambridge
- Rigaut F (2002) Ground-conjugate wide field adaptive optics for the ELTs. *Proc ESO* 58:1116
- Roddier F (1981) The effect of atmospheric turbulence in optical astronomy. *Prog Opt* XIX:281–376
- Roddier F (1999) *Adaptive optics in astronomy*. Cambridge University Press, Cambridge
- Roddier F, Roddier C (1988) Curvature sensing and compensation: a new concept in adaptive optics. *Appl Opt* 27:1223–1225
- Roggeman MC, Welsh B (1996) *Imaging through turbulence*. CRC Press, Boca Raton
- Sandler D, Cuellar L, Lefebvre M, Barrett T, Arnold R, Johnson P, Rego A, Smith G, Taylor G, Spivey B (1994) Shearing interferometry for laser-guide-star atmospheric correction at large  $D/r_0$ . *J Opt Soc Am A* 11:858873
- Sasiela RJ (2007) *Electromagnetic wave propagation in turbulence*. Society of Photo-Optical Instrumentation Engineers, Bellingham
- Skidmore W, Els S, Travouillon T, Riddle R, Schoeck M, Bustos E, Seguel J, Walker (2009) Thirty meter telescope site testing V: seeing and isoplanatic angle. *Publ Astron Soc Pac* 121:1151–1166
- Stetson P (1987) DAOPHOT—a computer program for crowded-field stellar photometry. *Publ Astron Soc Pac* 99:191–222
- Soummer R, Pueyo L, Larkin J (2012) Detection and characterization of exoplanets and disks using projections on Karhunen–Loève eigenimages. *Astrophys J Lett* 755:L28
- Talbot G et al (2006) GLAS: engineering a common-user Rayleigh laser guide star for adaptive optics on the William Herschel Telescope. *Proc Soc Photo Opt Instr Eng* 6272:62722H

- Tallon M, Foy R (1990) Adaptive telescope with laser probe—isonatism and cone effect. *Astron Astrophys* 235:549–557
- Tatarskii VI (1961) *Wave propagation in a turbulent medium*. McGraw-Hill, New York
- Taylor GI (1938) *Proc R Soc A* 164:476–490
- Thomas S, Adkins S, Gavel D, Fusco T, Michau V (2008) Study of optimal wavefront sensing with elongated laser guide stars. *Mon Not R Astron Soc* 387:173–187
- Thompson LA, Gardner CS (1987) Experiments on laser guide stars at Mauna Kea Observatory for adaptive imaging in astronomy. *Nature* 328:229–231
- Tokovinin AA (1988) A new method to measure atmospheric seeing. *Pis'ma v AZh* 24:768–771 (*Astron Lett* 662–664)
- Tokovinin A (2002) From differential image motion to seeing. *Pub Astron Soc Pac* 114:1156–1166
- Tokovinin A, Viard E (2001) Limiting precision of tomographic phase estimation. *J Opt Soc Am A* 18:873–882
- Tokovinin A, Kornilov V (2007) Accurate seeing measurements with MASS and DIMM. *Mon Not R Astron Soc* 381:1179–1189
- Tokovinin A, Bustos E, Berdja A (2010) Near-ground turbulence profiles from a lunar scintillometer. *Mon Not R Astron Soc* 404:1186–1196
- Tokovinin A, Kornilov V, Shatsky N, Voziakova O (2003) Restoration of turbulence profile from scintillation indices. *Mon Not R Astron Soc* 343:891–899
- Tokovinin A, Kellerer A, Coudé Du, Foresto V (2008) FADE, an instrument to measure the atmospheric coherence time. *Astron Astrophys* 477:671–680
- Tokovinin A, Travouillon T (2006) Model of optical turbulence profile at Cerro Pachón. *Mon Not R Astron Soc* 365:1235–1241
- Trinquet H, Vernin J (2006) A model of forecast seeing and estimate  $C_N^2$  profiles from meteorological data. *Pub Astron Soc Pac* 118:756–764
- Trippe S, Davies R, Eisenhauer F, Frster Schreiber NM, Fritz TK, Genzel R (2010) High-precision astrometry with MICADO at the European Extremely Large Telescope. *Mon Not R Astron Soc* 402:1126–1140
- Tyson RK (2000) *Introduction to adaptive optics*. Society of Photo-Optical Instrumentation Engineers, Bellingham
- Tyson RK (2011) *Principles of adaptive optics*. CRC Press, Boca Raton
- Tyson RK, Frazier BW (2004) *Field guide to adaptive optics*. Society of Photo-Optical Instrumentation Engineers, Bellingham
- Ulrich PB, (1988) Hufnagel-Valley profiles for specified values of the coherence length and isoplanatic patch angle. WJ Schafer Associates, WJSA/MA/TN-88-013, Arlington, Virginia
- Véran J-P (1997) Estimation of the adaptive optics long-exposure point-spread function using control loop data. *J Opt Soc Am A* 14:3057–3069
- Véran J-P, Fusco T, Clénet Y ed. (2012) Second international conference on adaptive optics for extremely large telescopes. <http://ao4elt2.lesia.obspm.fr>
- Vernin J, Roddier F (1973) Experimental determination of two-dimensional spatiotemporal power spectra stellar light scintillation. Evidence for a multiplayer structure of the air turbulence in the upper troposphere. *J Opt Soc Am* 63:270–273
- Vernet E, Ardiciaccon C, Baruffolo A, Diolaiti E (2005) Layer-oriented wavefront sensor for a multiconjugate adaptive optics demonstrator. *Opt Eng* 44:096601
- Wallace JK (2011) Common-path interferometric wavefront sensing for space telescopes. In: Aerospace conference, 2011 IEEE, pp 1–7
- Wang L, Otarola A, Ellerbroek B (2010) Impact of sodium laser guide star fratricide on multi-conjugate adaptive optics systems. *J Opt Soc Am A* 27:A19–A28
- Welsh BM, Ellerbroek BL, Roggemann MC, Penning TL (1995) Fundamental performance comparison of a Hartmann and a shearing interferometer wave-front sensor. *Appl Opt* 34:4186–4195
- Wilson RW (2002) SLODAR: measuring optical turbulence altitude with a Shack–Hartmann wavefront sensor. *Mon Not R Astron Soc* 337:103108
- Yaglom AM (1941) *Dan SSSR* 69:743–746
- Ziad A, Conan R, Tokovinin A, Martin F, Borgnino J (2000) From the grating scale monitor to the generalized seeing monitor. *Appl Opt* 39:5415–5425